

# Master Thesis

## Camera Based Detection and Localization of Noctilucent Clouds

submitted by

Manoj Raman Kondabathula

Matrikel: 215206956

Supervisor:

Prof. Dr.-Ing. N. Damaschke

Dr. G. Baumgarten

Dr.-Ing. M. Schaeper

Rostock, 11.05.2018

## Masterarbeit

für Herrn **Manoj Raman Kondabathula** (Matrikel-Nr. 215206956)

**Thema: Kamerabasierte Detektion und Lokalisierung von leuchtenden Nachtwolken (NLC)**  
**Camera Based Detection and Localization of Noctilucent Clouds (NLC)**

### Aufgabenstellung:

Das Leibniz-Institut für Atmosphärenphysik in Kühlungsborn (IAP) beobachtet NLC (noctilucent clouds) mit einem Kameranetzwerk an verschiedenen Standorten in Europa. Schwerpunkt aktueller Untersuchungen ist die Detektion und die Höhenbestimmung der NLC aus den Bilddaten. Die Höhenbestimmung wurde von verschiedenen Autoren mittels Triangulation durchgeführt, wobei die zu korrelierenden Bildmerkmale manuell ausgewählt wurden. Für eine systematische Beobachtung wäre es von Vorteil, das Auftreten von NLCs automatisch zu erfassen sowie eine automatisierte Höhenschätzung zu realisieren. Daneben sind Informationen zur Struktur und Bewegungsgeschwindigkeit von Interesse für das IAP.

Im Rahmen der Masterarbeit wird eine automatisierte Erkennung und Charakterisierung der NLCs anhand der vorliegenden Bilddaten angestrebt. Die folgenden Punkte sind in der Arbeit zu bearbeiten

- Einarbeitung in die Thematik und Einordnung der vorhandenen Untersuchungen und Literatur zur Detektion und Charakterisierung von NLCs
- Erstellung von Algorithmen zur Detektion von potentiell auswertbaren NLCs Bildern bzw. Bildbereichen
- Anpassung vorhandener Algorithmen zur Bestimmung der geometrischen Beziehungen der Triangulation
- Extraktion von Wolkenmerkmalen zur automatisierten Höhenbestimmung der NLCs, eventuell incl. Geschwindigkeits- und Strukturerkennung
- Konzeption eines Multi-Spektral-Kamerasystems mit den Komponenten des Instituts AE

**Tag der Ausgabe:** 01.12.2017

**Tag der Abgabe:** 11.05.2018

**Betreuer:** Prof. Dr.-Ing. N. Damaschke (Uni Rostock), Dr. G. Baumgarten (IAP)

# Index

Abstract .....	i
1 Introduction .....	1
2 Instruments and Data analysis .....	3
2.1 Camera network .....	3
2.2 Images of interest .....	4
2.3 Intensity distribution of the images .....	6
2.4 Colour ratios of the images .....	11
3 Detection of NLC .....	14
3.1 Template .....	14
3.2 Surface Similarity Parameter .....	15
3.3 Spatial filtering velocimetry .....	17
3.4 Choice of the grating function .....	19
3.5 Detecting structural movements in the Sky .....	21
4 Localization of NLC .....	23
4.1 Pinhole Camera model .....	23
4.2 Stereoscopy depth measurement .....	25
4.3 Homogeneous Coordinate Transformation .....	27
4.4 NLC range calculation .....	31
4.4.1 Coordinate system .....	31
4.4.2 Converting pixel position to azimuth and elevation .....	32
4.4.3 Estimating Latitude, Longitude and Altitude using Homogeneous Coordinate Transformations .....	33
4.4.4 Range from the camera's baseline .....	36
5 Summary & Outlook .....	39
5.1 Summary .....	39

5.2 Outlook.....	40
References. ....	41
Statutory declaration.....	43
Appendix A : .....	44

# Table of Figures

Figure 1.1 NLC observation geometry [Baumgarten, G 2009] .....	1
Figure 1.2 NLC observed from Kühlungsborn on 1st July 2017, at 23:06:50. ....	2
Figure 2.1: Layout of NLC camera network between 700N and 370N [Baumgarten, G 2009]. The red dot indicates the location of Kühlungsborn and the blue dot indicates the location of IOW. Grey shaded regions show the field of view of the cameras. ....	3
Figure 2.2 (a): Total number of images captured between 00 and -200 solar elevation angle. (b): Total number of NLC images observed manually between 00 and -200 solar elevation angle. [Baumgarten, G 2009] .....	5
Figure 2.3: Mean NLC occurrence frequency for the peak NLC season (left: DFS=0–50) and the late NLC season (right: DFS=30–60) during summer 2007 and 2008. Top: Occurrence frequency observations against solar elevation angle. Bottom: Occurrence frequency against local solar time. Please note that the observations at Pic du Midi are rescaled by a factor of three. [Baumgarten, G 2009] .....	5
Figure 2.4: Top: Minimum solar elevation angle for the different camera locations. Bottom left: NLC visibility throughout the season. Bottom right: Seasonal average NLC visibility throughout the day (averaged only for days with the solar elevation below -50). [Baumgarten, G 2009] .....	6
Figure 2.5: Normalised mean vertical intensity of a clear sky. Image from Kühlungsborn 2015-06-06 21:39:49. Solar elevation -10.69. Note that the vertical pixel number is roughly proportional to the elevation angle. The elevation angle is roughly 25° at pixel 0, and 0.8° at pixel 2700. ....	7

Figure 2.6: Normalised mean vertical intensity distribution of clear sky images with different ISO settings.....	8
Figure 2.7: Normalised mean vertical intensity distribution of clear sky images after compensation. The $CP$ values are given in the legend. ....	9
Figure 2.8: Normalised intensity distribution comparison between the reference image and the test image. The intensity drops in the test image from pixels around 2000 to 2300 due to the presence of lower atmospheric clouds. ....	10
Figure 2.9: Normalised intensity distribution comparison between the reference image and the test image. A peak in intensity followed by a dip can be observed in the test image from pixel 1400 to 2200 due to the presence of NLC. Also, an effect of constant scaling factor can be observed from pixels 0 to 1300. ....	10
Figure 2.10: The ratio of intensities of a column from the reference image and clear sky test image.....	11
Figure 2.11: Colour ratios comparison between one column of pixels from a clear sky and the reference image. ....	12
Figure 2.12: Colour ratios comparison between one column of pixels from the image with lower atmospheric cloud and the reference image. The shift in the mean distribution towards (0.2,0.5) indicates a rise in intensity of Red colour and Green colour.....	12
Figure 2.13: Colour ratios comparison between one column of pixels from the image with NLC and the reference image. The shift in the mean distribution towards (2.5,1.5) indicates a rise in intensity of Blue colour and decrease in Red colour. ....	13
Figure 3.1: Clear sky Template for -100 solar elevation during sunrise. The template formed by combining around 440 images from Kühlungsborn.	

Template size: 7100x2700 pixels, single image size: 5184x2700 pixels.  
Solar azimuth range 4.9O to 17.7O ..... 15

Figure 3.2: Image captured from Kühlungsborn on July 3, 2017, at 00:26:19 UT converted to grey scale. The surface similarity between the reference image and the test image is calculated, and regions where the value is higher than 0.25, are masked (Black colour)..... 17

Figure 3.3: A moving surface is projected on to pixel grid by a focusing lens [M Schaeper 2013]. The grating is applied by multiplying the grating function. Here, the grating is -1 and +1, all odd rows/columns are added together and all even rows/columns are added together, and the difference of these two sums gives the spatial filter signal. Applying grating along rows and columns facilitates 2D velocity measurement. .... 19

Figure 3.4: Fourier coefficients along the x-axis. Fourier coefficient  $m_0 = 23$  is considered for the desired grating period..... 21

Figure 3.5: The amplitude ( $A$ ) of the signal ( $S$ ) for two images from Kühlungsborn on July 10th, 2015 (21:09:53 and 21:10:33 UT). The gray scale is proportional to  $S$  and ranges from 0 to  $2.5e8$ . A minimum threshold amplitude  $A = 400$  is used to mask the image. The bright regions of the image represent the presence of NLC. .... 22

Figure 4.1: Simple illustration of a pinhole camera model. The light from outside world enters a closed box through an infinitesimally small hole and projects an inverted image on the photosensitive wall..... 23

Figure 4.2: The 3D geometry of a pinhole camera model depicting the projection of global point P on to the image plane at point  $p$ ..... 24

Figure 4.3: Projection along XZ plane of the pinhole camera model. The red shaded region is the outside world, and the blue shaded region is inside pinhole camera..... 24

Figure 4.4: Ideal alignment of two cameras separated by a distance ( $d$ ) observing a point ( $P$ ) in the 3D world. The field of view is indicated by shaded areas. Red lines represent the optical axis of the camera.....	26
Figure 4.5: Simple layout of the projection of point $P$ on to the image plane of both cameras using pinhole camera model. ....	27
Figure 4.6: Representation of pure coordinate translation from origin $O$ to $O'$ by an amount of $a$ , $b$ , and $c$ along $X$ , $Y$ , and $Z$ axes respectively. ....	29
Figure 4.7: Transformation of the frame of reference from $\mathcal{F}0$ to $\mathcal{F}k$ by multiple translation and rotations [Briot S & khalil W 2015].....	31
Figure 4.8: An oblate surface model of Earth. Earth Centred Earth Fixed coordinates in relation to latitude and longitude. The origin is located at the centre of mass of earth. $a$ is semi-major axis, $b$ is semi-minor axis, $\varphi$ is latitude, $\lambda$ is longitude, X-Y-Z is ECEF coordinate system, and E-Up-N is local ENU coordinate system.....	32
Figure 4.9 Left: Top view of local coordinate system ENU. Right: Sided view of ENU. The blue point indicates the position of the NLC.....	35
Figure 4.10: Searching for the NLC structure in an integration area selected around the initially approximated pixel. The black dot indicates the initial pixel position. Green colour indicates first step and the red colour indicates the second step. ....	37



# Abstract

This thesis work is aimed at automatic detection of Noctilucent Clouds from sky images and also to detect their range to the observer. The cameras used are from the Trans-European Network of Cameras for Observation of Noctilucent Clouds [Baumgarten 2009] developed by the Leibniz-Institute of Atmospheric Physics e.V. (IAP) at the Rostock University, Kühlungsborn, Germany. This network of cameras continuously captures sky images resulting in an extensive database and requires time-consuming effort to classify the images with Noctilucent Clouds. The motivation is to reduce the manual burden and to extract maximum possible information from the images instead of simple classification. Previous attempts have been made to detect the presence of NLC from images using KNN (k-Nearest Neighbors) algorithm [Schmidt 2013] and to detect the altitude of NLC by solving the geodesic problem [Schaefer 2016]. The aim of this thesis is similar, but with a different approach for faster, better and automatic detection of NLC, and also to calculate their altitude by detecting an accurate position of the NLC structure in the image.

Section 2 describes the available infrastructure and properties of the images in detail. Section 3 presents a description of the spatial filtering technique with a complex grating function and a surface similarity parameter along with the implementation of the duo for the detection of the NLC. The range of the NLC is calculated using the phase output from spatial filtering technique as a disparity parameter in the triangulation. The pinhole camera model and homogeneous coordinate transformations are also applied alongside with triangulation in Section 4 to provide clear documentation of the underlying processing steps.

# 1 Introduction

Noctilucent Clouds are brilliant atmospheric phenomenon formed by water ice nanoparticles in the upper mesosphere of Earth's atmosphere. These clouds form at an altitude of about  $83 \pm 1$  KM [Jesse. O 1896, Witt. G 1962] in the northern hemisphere during local summer when the temperatures reach a range of 120 Kelvin to 150 Kelvin [Rapp, M. & Thomas, G. E. 2006]. The ground-based observation of the Noctilucent clouds is possible when the Sun is below the horizon shading off the lower atmospheric clouds but illuminating the Noctilucent Clouds in higher altitudes. However, the visibility of NLC may go beyond the geometrical horizon due to atmospheric refraction. They were first observed in 1885 and early photographed by Mr Otto Jesse in 1887. Ever since then, Noctilucent Clouds were extensively observed to understand the physical properties of the atmosphere. The Trans-European Network of Cameras for Observation of NLC by IAP is one such ground observation facility.

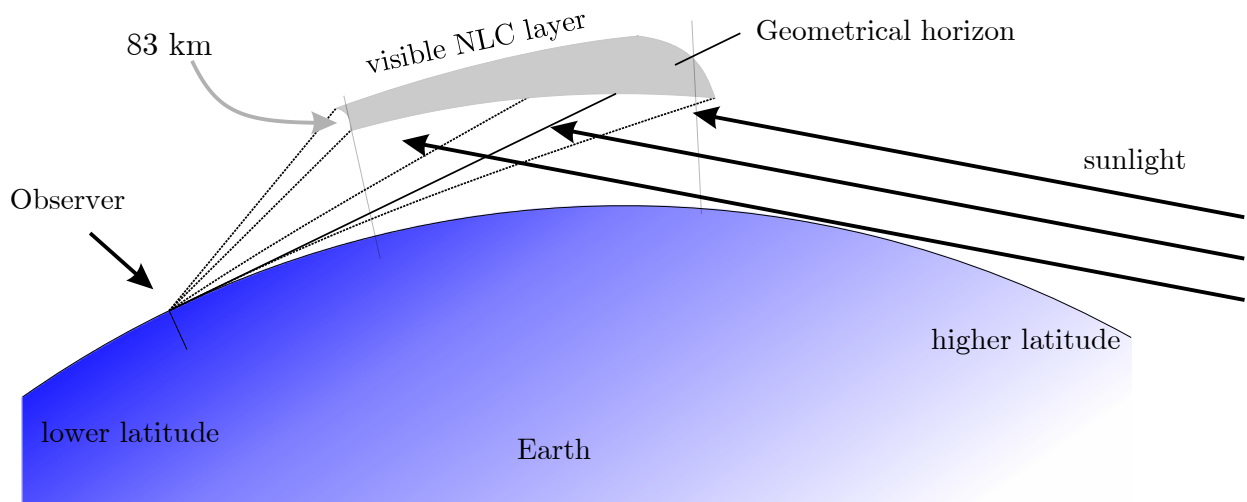


Figure 1.1 NLC observation geometry [Baumgarten, G 2009]

The formation of NLC is assumed to be dependent on global atmospheric dynamics [Thomas G E 1989, Zahn U 2003], and henceforth many parameters are calculated using different observations from ground and space. Active sounding by light detection and ranging (Lidar) is a recently popularised method for ground-based observation.

The structures of the Noctilucent clouds are the measures of the atmospheric gravity waves that become visible due to the presence of NLC and appear on scales that are not accessible by any other methods. The analysis of these structures with respect to horizontal scales and temporal evolution allows quantifying the gravity wave parameters. The larger interest in detecting the presence of NLC is to perform combined lidar and high-resolution camera observations automatically.



Figure 1.2 NLC observed from Kühlungsborn on 1<sup>st</sup> July 2017, at 23:06:50.

Due to the vast variations in the colour spectrum of NLC, a process purely dependent on such a measure of the sky gives unsatisfactory results. However, the intensity variations of the sky provide a scale to identify and separate lower atmospheric clouds. The Noctilucent Clouds are known for their structural properties formed by the effect of gravity waves in the atmosphere, a detection process using such invariant properties of NLC could produce reliable results.

## 2 Instruments and Data analysis

### 2.1 Camera network

A network of more than ten high-resolution digital cameras installed between ALOMAR (69°N,16°E) and Calar Alto (37.2°N, 2.6°W) for the observation of NLCs. They are used to identify suitable science conditions for rocket soundings and lidar observations and also to compare the horizontal structures of NLC with the results from sounding observations. The camera observations are available for the scientific community and the public to facilitate detailed study.

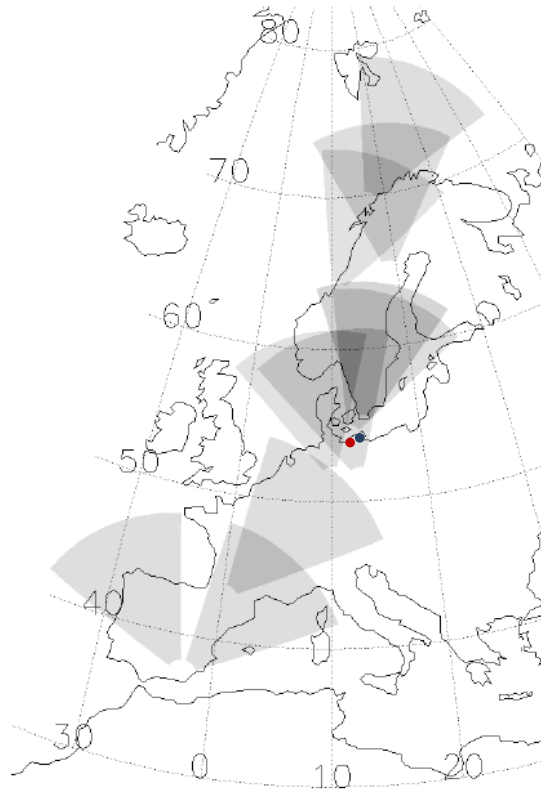


Figure 2.1: Layout of NLC camera network between 70°N and 37°N [Baumgarten, G 2009]. The red dot indicates the location of Kühlungsborn and the blue dot indicates the location of IOW. Grey shaded regions show the field of view of the cameras.

The cameras operate automatically, a software adjusts exposure time, sensitivity and aperture settings of the cameras. During the twilight period, the software calculates the brightness histogram of the pixels in the twilight region from the previous image

and determines the camera settings to capture maximum dynamic range of the sky radiation. For the better life of the cameras, the imaging frequency is determined based on the solar elevation angle. The cameras between  $51^{\circ}\text{N}$  and  $69^{\circ}\text{N}$  roughly face towards the true North. The field of view (FOV) of the cameras is large enough to cover both sunrise and sunset. At lower latitudes,  $43^{\circ}\text{N}$ , the cameras look towards sunrise and at  $37^{\circ}\text{N}$  two cameras were installed looking towards dawn and dusk. The cameras used are Canon EOS 550D with a sensor size of 22.3 mm x 14.9 mm and 18Mp resolution covering approximately  $47^{\circ}$  horizontal-FOV and  $31^{\circ}$  vertical-FOV.

During the NLC season, roughly 7GB of compressed data is generated per day and transferred to IAP in real time over the internet. These images are analysed to determine the detection efficiency of NLC in relation with elevation and day of the year.

## 2.2 Images of interest

To understand the occurrence and observability of the NLC over 750,000 images from the camera network are observed during the NLC season roughly between 1<sup>st</sup> of May and 30<sup>th</sup> of August 2007 and 2008. Out of which over 24,000 images are manually identified with NLC (see Figure 2.2).

The NLC occurrence rate is calculated by dividing the total number of images with observed NLC images within the respective categories of  $1^{\circ}$  solar elevation steps. These results show a high chance of NLC observation between  $-8^{\circ}$  and  $-14^{\circ}$  of solar elevation (see Figure 2.3) [Baumgarten G 2009]; this result is different from previous observations [Gadsden M & Schröder W 1989] who found the peak of observation between  $-6^{\circ}$  and  $-16^{\circ}$ . The visual observability of the NLC strictly depends on solar elevation. The brighter and structured NLC can be identified even during higher solar elevation, but to identify weak structures, the background sky should be darker. From the observation in [Baumgarten G 2009] images between  $-5^{\circ}$  and  $-17^{\circ}$  solar elevation is considered as the desired illumination conditions for the observability of the NLC.

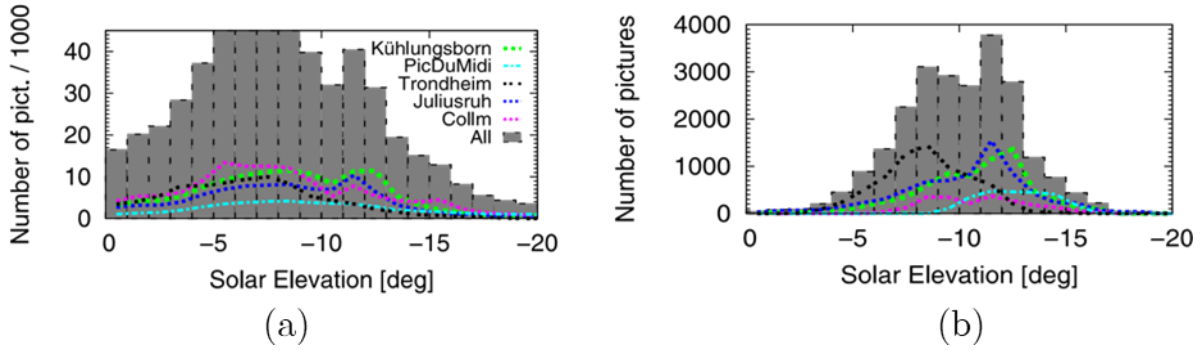


Figure 2.2 (a): Total number of images captured between  $0^{\circ}$  and  $-20^{\circ}$  solar elevation angle. (b): Total number of NLC images observed manually between  $0^{\circ}$  and  $-20^{\circ}$  solar elevation angle. [Baumgarten, G 2009]

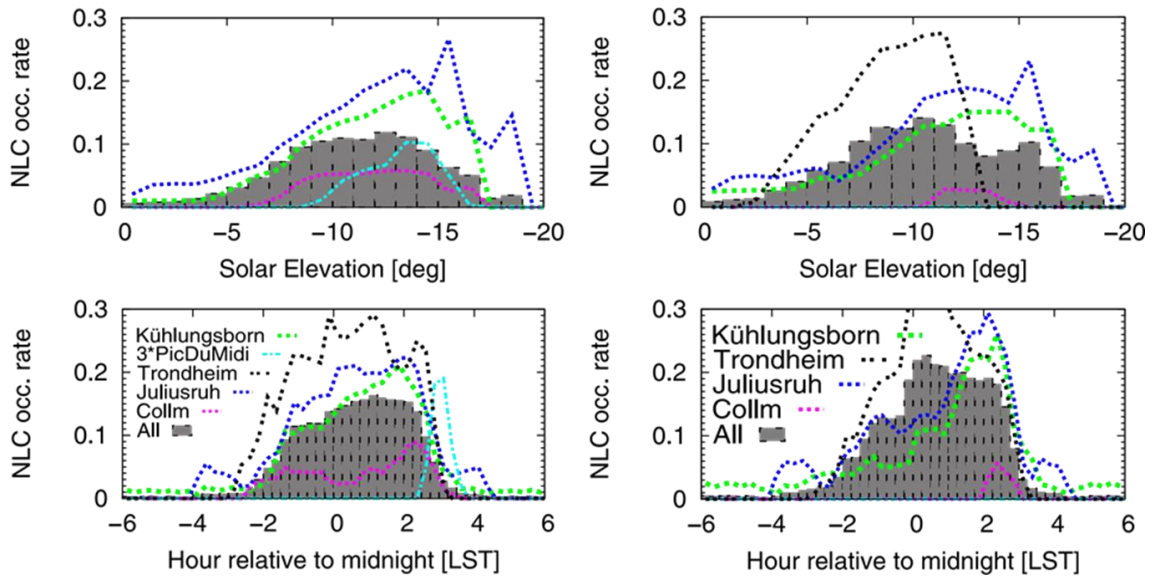


Figure 2.3: Mean NLC occurrence frequency for the peak NLC season (left: DFS=0–50) and the late NLC season (right: DFS=30–60) during summer 2007 and 2008. Top: Occurrence frequency observations against solar elevation angle. Bottom: Occurrence frequency against local solar time. Please note that the observations at Pic du Midi are rescaled by a factor of three. [Baumgarten, G 2009]

The lowest solar elevation depends on the latitude of the camera, at  $64^{\circ}$  N,  $55^{\circ}$  N,  $54^{\circ}$  N the lowest solar elevation is  $-10^{\circ}$ ,  $-15^{\circ}$ ,  $-14^{\circ}$  respectively. The comparison between the latitude of the camera and better visibility is made by the ratio of time between  $-5^{\circ}$  and  $-17^{\circ}$  solar elevation and total time of the day. This result (Figure 2.4) shows the highest visibility of about 27% per day between Days from solstice (DFS) -50 to +50 for latitudes between  $51^{\circ}$  N and  $59^{\circ}$  N and decreases with latitude. At  $55^{\circ}$  N the

NLC visibility is around 25%, at  $51^\circ$  N it decreases to less than 5% and further down at  $43^\circ$  N the visibility is less than 4%. Based on the finding that Kühlungsborn ( $54^\circ 07' 01.0''$ N  $11^\circ 46' 19.4''$ E) is located in a latitude band favourable for NLC observations another camera was set up in Warnemünde ( $54^\circ 10' 45.9''$ N  $12^\circ 04' 52.4''$ E) close to Kühlungsborn.

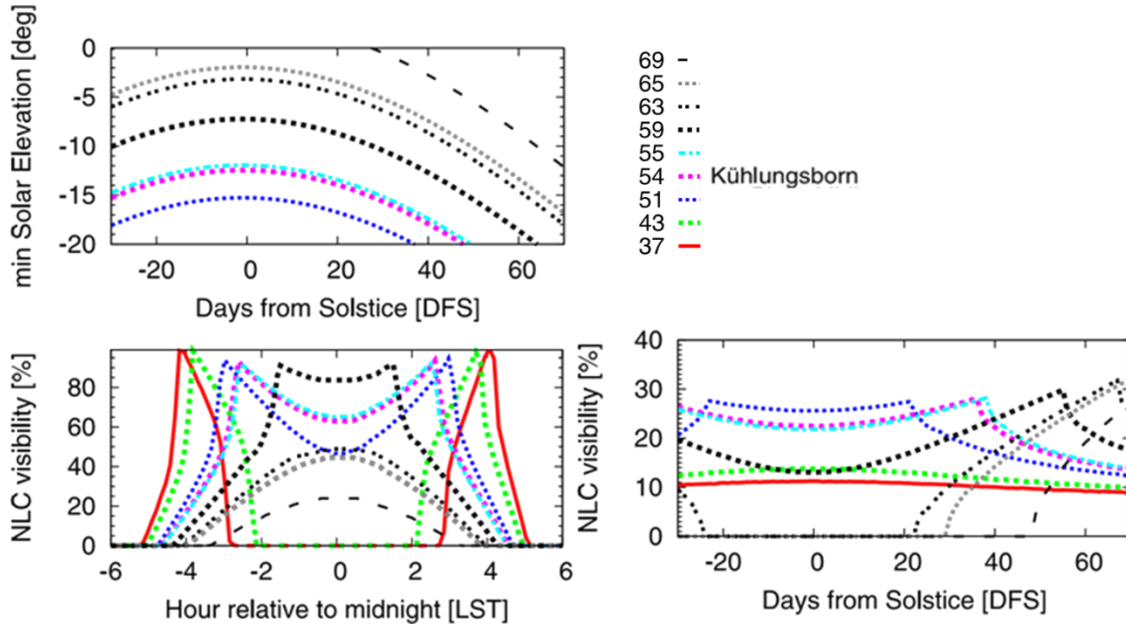


Figure 2.4: Top: Minimum solar elevation angle for the different camera locations. Bottom left: NLC visibility throughout the season. Bottom right: Seasonal average NLC visibility throughout the day (averaged only for days with the solar elevation below  $-5^\circ$ ). [Baumgarten, G 2009]

### 2.3 Intensity distribution of the images

About 210,000 images from Kühlungsborn between 1<sup>st</sup> of May and 31<sup>st</sup> of August 2015 to 2017 were manually inspected, and roughly 17,000 clear sky images and 2,000 NLC images were identified. The clear sky images are used for comparison with the image of interest (test image) to detect lower atmospheric clouds and mark them. In the second step, the NLC images are used as test images.

It is also essential to understand the colour properties and intensity distribution of images to establish a threshold to identify pixels belonging to the clear sky, dark clouds and NLC. The intensity distribution ( $I_g$ ) [Equation 2.3.1] of a clear sky is analysed by

taking mean values of each pixel row ( $r$ ) of the image ( $i$ ) and normalising the values of the resulting column to one (Figure 2.5). This shows that the vertical intensity distribution increases exponentially with a decrease in elevation up to the twilight region and then the intensity decreases further below the twilight region.

$$I_g = \frac{\sum_{r=1}^n i_r}{\max(\sum_{r=1}^n i_r)}$$

2.3.1

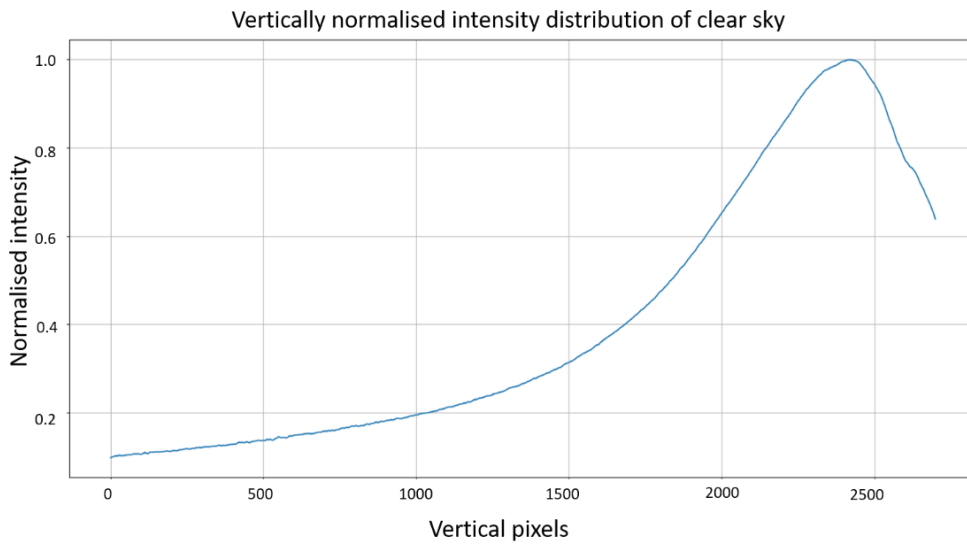


Figure 2.5: Normalised mean vertical intensity of a clear sky. Image from Kühlungsborn 2015-06-06 21:39:49. Solar elevation  $-10.69^\circ$ . Note that the vertical pixel number is roughly proportional to the elevation angle. The elevation angle is roughly  $25^\circ$  at pixel 0, and  $0.8^\circ$  at pixel 2700.

The presence of NLC increases the overall brightness of the sky which results in lower exposure time, lower sensitivity and smaller aperture value, while the presence of dark lower atmospheric clouds decreases the overall intensity. The camera network software automatically controls the camera settings such that fewer pixels are underexposed or overexposed. Higher sensitivity or higher ISO value and longer exposure time result in a non-linear signal to noise ratio of the sensor, this can be seen as a result of variation in the vertical intensity distribution for different clear sky images (during similar solar elevation) with different ISO values as shown in Figure 2.6. The intensity characteristics of the camera for red, blue and green colour channels for different sensor sensitivity and exposure settings (images attached in Appendix A) reveals a slight



variation in the intensity, which means that the camera is more sensitive to one colour than to other colour.

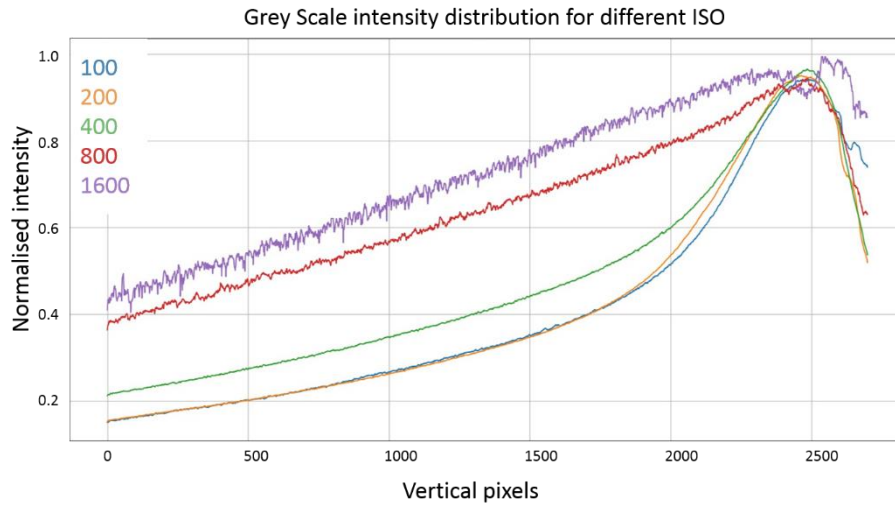


Figure 2.6: Normalised mean vertical intensity distribution of clear sky images with different ISO settings.

An increase in exposure time and aperture diameter also affect sensor characteristics, to observe the same, a camera compensation parameter ( $CP$ ) is formulated in terms of exposure time ( $E_t$ ), sensitivity ( $ISO$ ) and aperture value ( $A$ ). By multiplying the intensity of the image with their respective  $CP$ , all images can be approximately compared.

$$CP = \frac{1}{E_t \frac{ISO}{100}} 2^{\frac{\log A}{\log(\sqrt{2})}}$$

2.3.2

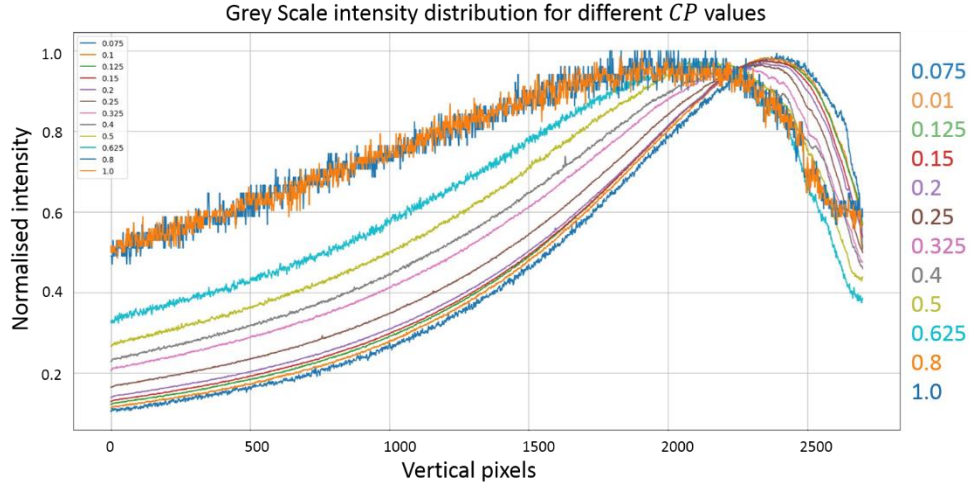


Figure 2.7: Normalised mean vertical intensity distribution of clear sky images after compensation. The  $CP$  values are given in the legend.

The compensation parameter helps to understand the combined non-linear effect of the camera sensor due to changes in exposure time, sensitivity and aperture. From the Figure 2.7, it can be noted that a higher compensation factor results in higher non-linearity of the sensor. From these observations, images with  $CP > 2.25$  are omitted for further investigations and calculations. The non-linearity problem is not eliminated by ignoring these images, but it is minimised.

The normalised intensity distribution of all columns of a clear sky image is similar to the overall vertical intensity distribution of the image. Human inspection can easily identify the variation in intensities in the column with the dark cloud (Figure 2.8) or NLC (Figure 2.9) in comparison with a reference image constructed by taking the mean of few clear sky images (only images with similar solar elevation angles are considered). This comparison is performed quantitatively by calculating the ratio of the reference image intensity distribution and the test image intensity distribution. The slope of the ratio should be zero in case of clear sky, negative in case of dark cloud and positive in case of NLC. However, the slope of the ratio of the reference image and the clear sky image is not always zero (see Figure 2.10). This could be due to the non-linear scaling factor of the sensor as the camera settings are different for the reference image and the test image.

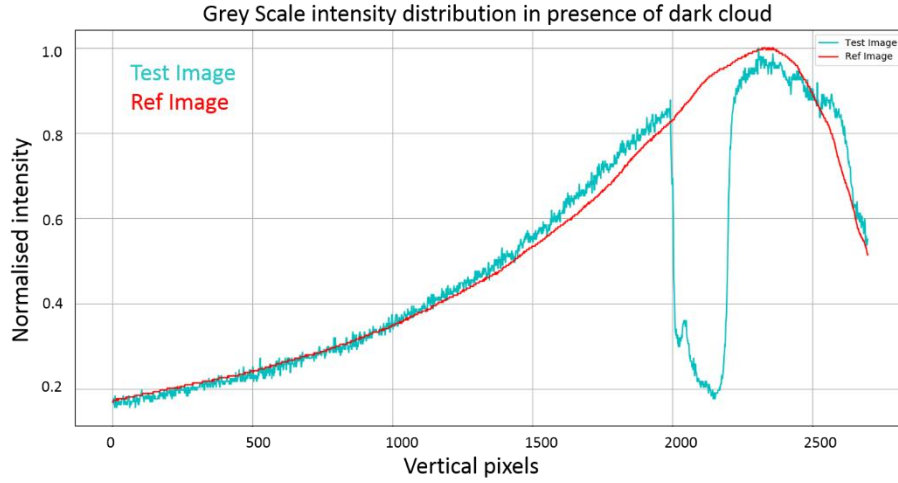


Figure 2.8: Normalised intensity distribution comparison between the reference image and the test image. The intensity drops in the test image from pixels around 2000 to 2300 due to the presence of lower atmospheric clouds.

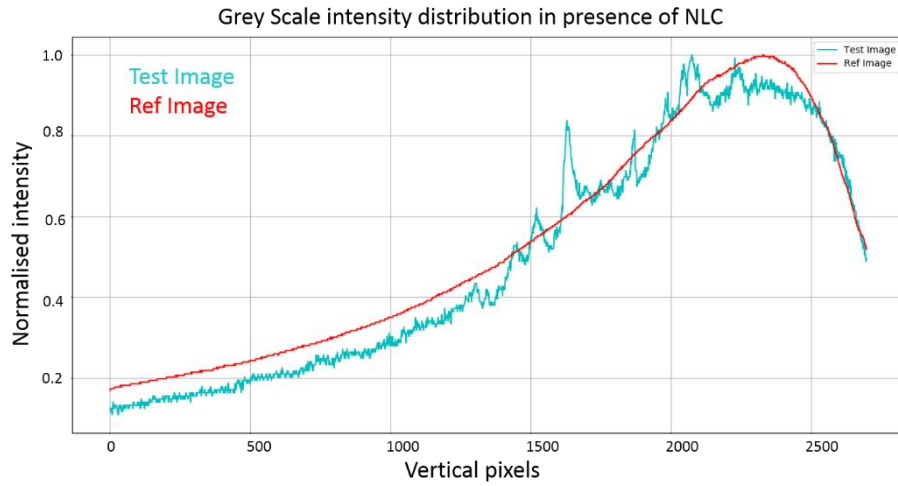


Figure 2.9: Normalised intensity distribution comparison between the reference image and the test image. A peak in intensity followed by a dip can be observed in the test image from pixel 1400 to 2200 due to the presence of NLC. Also, an effect of constant scaling factor can be observed from pixels 0 to 1300.

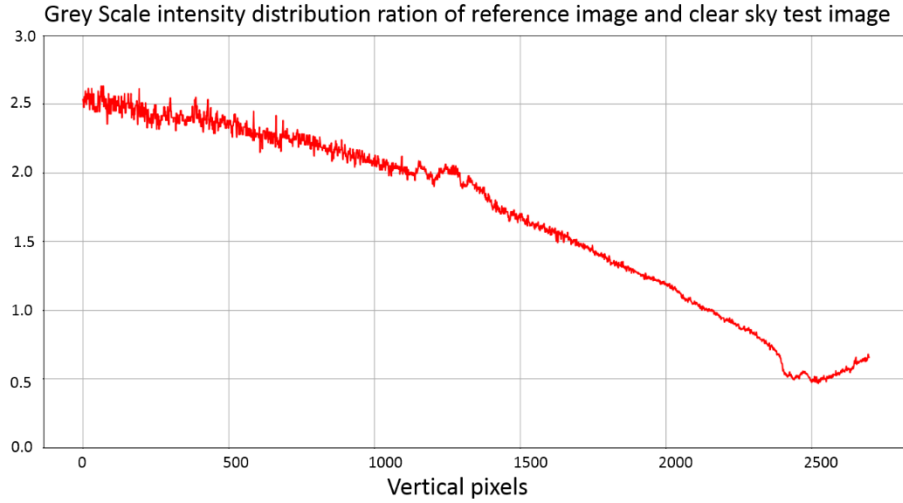


Figure 2.10: The ratio of intensities of a column from the reference image and clear sky test image.

These observations help to identify suitable clear sky images to form the templates for further investigation. Furthermore, it shows that the absolute variation of intensity due to the presence of lower atmospheric clouds is much higher than variations due to the presence of NLC. This means it is possible to identify the pixels belonging to the lower atmosphere clouds with good efficiency using a threshold cut off. However, the threshold measurement should be immune to changes in sensor nonlinearity.

## 2.4 Colour ratios of the images

The presence of the NLC and the lower atmospheric clouds in an image changes the spectral properties of the images drastically; these can be observed from the relation between colour ratios (Green/Blue and Red/Blue). The colour ratios of the pixel values from similar column position of clear sky, NLC and the lower atmospheric clouds in comparison with the colour ratios of a reference image (also during similar solar elevation period) are shown in Figure 2.11, Figure 2.12, Figure 2.13.

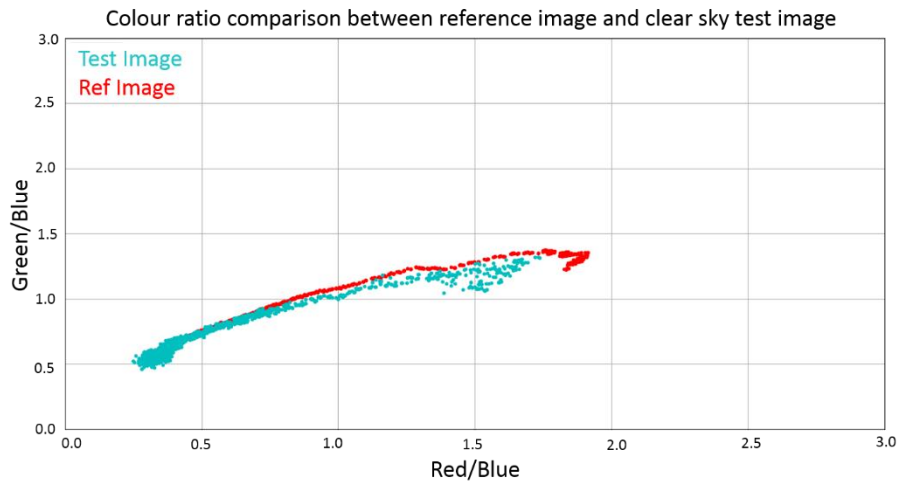


Figure 2.11: Colour ratios comparison between one column of pixels from a clear sky and the reference image.

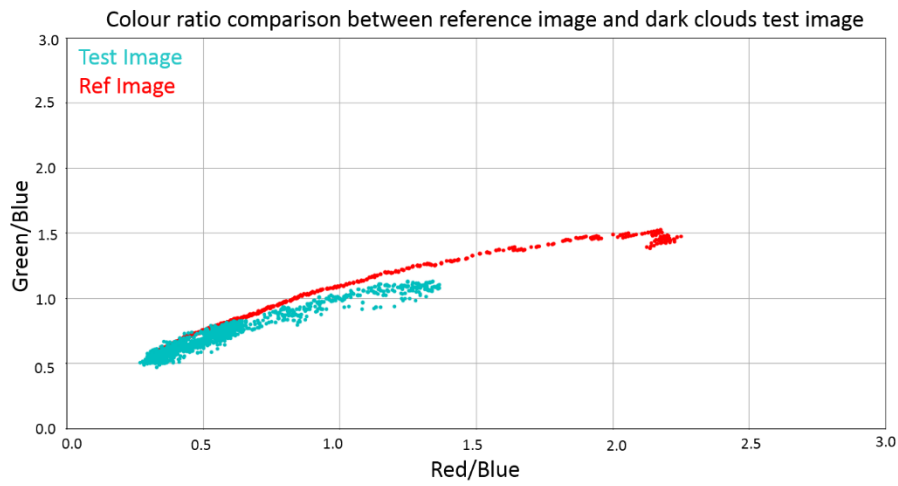


Figure 2.12: Colour ratios comparison between one column of pixels from the image with lower atmospheric cloud and the reference image. The shift in the mean distribution towards (0.2,0.5) indicates a rise in intensity of Red colour and Green colour.

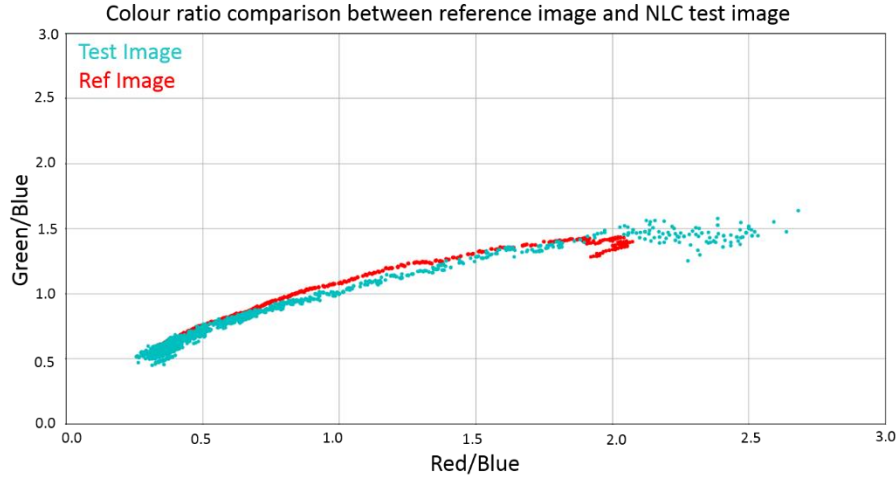


Figure 2.13: Colour ratios comparison between one column of pixels from the image with NLC and the reference image. The shift in the mean distribution towards (2.5,1.5) indicates a rise in intensity of Blue colour and decrease in Red colour.

Figure 2.12 shows that the pixels belonging to dark clouds have more Red and Green component and less Blue component compared to the reference image and Figure 2.13 shows that the pixels belonging to NLC have less red component and more Blue and Green component compared to the reference image. It shows that the Euclidean distance between colour ratios of the test image and reference image of same pixel position gives a measure of similarity to the clear sky conditions. However, the colour ratios alone cannot be used to distinguish between lower atmospheric cloud and the NLC as the effect of non-linear characteristics makes it much difficult to arrive at a fixed threshold value to identify dark clouds and NLC.

### 3 Detection of NLC

#### 3.1 Template

The NLC often show periodic structures caused by the gravity waves in the atmosphere, the propagation of gravity wave results in the movement of structures in the NLC, while the particles forming the NLC are affected by the wind. This phenomenon can be interpreted as a motion of a periodic structure over a constant background and can be detected with spatial filtering velocimetry (SFV) techniques [M Schaeper & N Damaschke 2017]. The presence of lower atmospheric clouds affects the SFV signal, to minimise their effect, the pixels of the image with lower atmospheric clouds need to be masked before SFV calculations. To determine the mask of non NLC pixels, clear sky reference images are required for comparing similarities with the test images as described in section 2.

The change in the position of the Sun affects the intensity distribution of the background sky, leading to an extensive database of the clear sky images. To the database, mean templates for each  $1^\circ$  step of solar elevation angle are constructed. The templates are formed by assuming no change in vertical illumination of the sky during the respective interval. The variation of intensity along the azimuth is compensated by shifting the images such that each pixel in the template is at the same horizontal distance from the Sun as such in the original image and normalising the mean intensities of each column to one. A moving average along each column of the template is calculated before normalising to acquire a smoothly varying intensity template. This procedure results in the normalised mean image of the sky for an interval of  $1^\circ$  solar elevation.

The horizontal distance mentioned in the previous paragraph is measured in number of pixels. The ratio of the horizontal resolution of the camera and horizontal field of view of the camera gives a parameter to scale pixels per degree. Multiplying this parameter by the difference of the Sun's azimuth angle and azimuth of the centre pixel

of the image gives the distance of the Sun to the centre of the image in pixels. This distance determines the position of the image in the template. To pick the relevant portion of the template for comparing with a test image, the solar azimuth angle of the test image and the farthest azimuth angle of the template are required.

The images considered for the construction of templates are based on the observations from section 2.2. Different templates are formed with images of different ISO values to make a reliable template. Intensities of each image are multiplied by the respective compensation parameter [Equation 2.3.2] before including the image in the calculation of the mean template. Two different sets of templates are formed: one for Sunrise and the other for Sunset as the azimuth position are very different, and the atmospheric composition that is responsible for the colour of the sky is different.



Figure 3.1: Clear sky Template for  $-10^\circ$  solar elevation during sunrise. The template formed by combining around 440 images from Kühlungsborn. Template size: 7100x2700 pixels, single image size: 5184x2700 pixels. Solar azimuth range  $4.9^\circ$  to  $17.7^\circ$

### 3.2 Surface Similarity Parameter

From the investigations described in sections 2.3 and 2.4, it became clear that it is difficult to estimate a fixed threshold value depending on intensity or ratios of colour intensities to gauge each pixel due to the nonlinearity of the sensor. A surface similarity parameter (SSP) as described by [Marc Perlin & Miguel D Bustamante 2014] is used. We applied the Sobolev Norm difference of two signals giving a quantitative measure



considering the amplitudes in the spatial frequency domain and phases of the two images.

The Sobolev norm  $\|f(\cdot)\|$  of a signal  $f(t)$  is [L. C. Evans 1998].

$$\|f(\cdot)\|^2 = \int_{-\infty}^{+\infty} |F(\omega)|^2 (1+|\omega|^2)^k d\omega \quad 3.2.1$$

In Equation 3.2.1,  $F(\omega)$  is the Fourier transform of the signal  $f(t)$ . The weighing factor  $(1+|\omega|^2)^k$  weights higher frequencies heavily depending on the  $k$  value.  $k$  is set to zero to weight all frequencies equally. The squared difference of the Sobolev norm of two signals gives a quantitative comparison. The error ( $E$ ) can be estimated from Equation 3.2.2.

$$E^2 = \|f_1(\cdot) - f_2(\cdot)\|^2 = \int |F_1(\omega) - F_2(\omega)|^2 d\omega \quad 3.2.2$$

The effect of a common scaling factor in image intensity caused due to changes in camera settings is eliminated by applying triangle inequality to normalise Equation 3.2.2.

$$Q(f_1, f_2) = \frac{(\int |F_1(\omega) - F_2(\omega)|^2 d\omega)^{1/2}}{(\int |F_1(\omega)|^2 d\omega)^{1/2} + (\int |F_2(\omega)|^2 d\omega)^{1/2}} \quad 3.2.3$$

If the two signals are entirely similar the difference of Fourier coefficients becomes zero and the similarity parameter becomes zero, and if both the signals differ entirely then the parameter becomes one.

For the detection of lower atmospheric clouds, the SSP from Equation 3.2.3 is calculated between the template image and the test image, to increase the accuracy of the parameter larger area of the images need to be compared, but this results in low detection resolution of the dark clouds. A trade-off is needed between resolution and accuracy. For the image in Figure 3.2, an area of 16x16 pixels is compared between the template and the test image. In regions of the dark clouds, the SSP is observed to be higher than 0.3 for most of the images. With about 75% match using an SSP threshold

of 0.25, the dark clouds are significantly masked. The remaining area is either clear sky or NLC.



Figure 3.2: Image captured from Kühlungsborn on July 3, 2017, at 00:26:19 UT converted to grey scale. The surface similarity between the reference image and the test image is calculated, and regions where the value is higher than 0.25, are masked (Black colour).

### 3.3 Spatial filtering velocimetry

The spatial filtering velocimetry technique was invented by Ator in 1963 to determine the velocity of a moving surface. It uses optical transmission grating between the sensor and observed scene to generate an oscillating signal whose frequency indicates the velocity of the dominant frequency spectrum in the observed scene [Ator 1963]. This technique is widely used for velocity measurements in fluid flow because of the advantage of in-situ and contact-free measurement and also due to the low-cost instruments compared to Laser Doppler techniques or Particle Image Velocimetry [Albrecht 2003 & Raffel 2007]. Many different methods are proposed for different applications using spatial filtering to determine fluid flows [Hosokawa & Tomiyama 2011, Matsumoto 2012] and surface velocity measurements [Sakai 1995, Schaeper 2016]. An application of spatial filtering technique to detect a moving structure in sky images and later to calculate the range of the structure from the baseline between the two cameras is described in this thesis.

The moving surface is projected on to the image plane through a grating filter by a lens; it can also be interpreted as weighting the image with a function describing the grating filter. For the 1-D velocity ( $v$ ) measurement of an intensity distribution along the  $x$  axis in an image  $i(x)$  (temporally represented as  $i(x-vt)$ ), is weighted with a grating function ( $g(x)$ ). The integration of the whole image results in the spatial filter signal ( $s(t)$ ) [M Schaeper 2008, M Schaeper & N Damaschke 2017].

$$s(t) = \int_{-\infty}^{+\infty} i(x-vt)g(x) \quad 3.3.1$$

For digital cameras, the image area depends on the number of pixels. Hence Equation 3.3.1 can be rewritten as Equation 3.3.2 where  $g(n)$  is the weighting factor of each pixel.

$$s(t) = \sum_{n=1}^p i(x-vt)g(n) \quad 3.3.2$$

The advantage of digital imaging is the possibility of generating virtual grating functions according to the user requirement to weight the pixels based on the spectral properties of the observed scene. Figure 3.3 shows an example of a grating filter setup. An equal number of pixels are periodically weighted with +1 and -1 such that the integral of the entire image is free from the background intensity and the output signal represents the motion of the object in the image.

The spatial filter generates a periodic signal in time that depends on the grating function. The velocity of the moving object can be represented with a dominant frequency ( $f_0$ ) of the spatial filter signal, the period of the grating function ( $g_p$ ) and the magnification ( $M$ ) of the lens.

$$v = \frac{f_0 g_p}{M}$$

Two-dimensional velocity measurements can be achieved by using a secondary grating function orthogonal to the primary grating [Bergeler and Krambeer 2004; Aizu and

Asakura 2006] resulting in two spatial filter signals  $S_x(t)$  and  $S_y(t)$ . This is visualised in Figure 3.3.

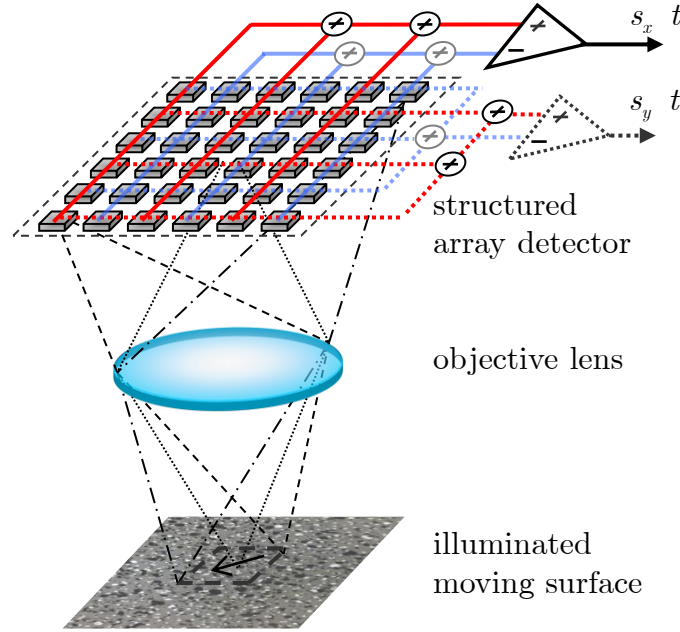


Figure 3.3: A moving surface is projected on to pixel grid by a focusing lens [M Schaeper 2013]. The grating is applied by multiplying the grating function. Here, the grating is -1 and +1, all odd rows/columns are added together and all even rows/columns are added together, and the difference of these two sums gives the spatial filter signal. Applying grating along rows and columns facilitates 2D velocity measurement.

### 3.4 Choice of the grating function

The spatial filter signal can be written as a complex time-dependent signal ( $s(t)$ ) using orthogonal sine and cosine grating functions which are direction sensitive and can be used to detect the velocity direction [Nomura 1996, Michel 1998b].

$$s(t) = \int_{-\infty}^{+\infty} i(x-vt)e^{-jkx} dx, \text{ spatial angular frequency } k = \frac{2\pi}{g_p} \quad 3.4.1$$

This signal  $s(t)$  can be interpreted as a single time-dependent Fourier coefficient  $c_k(t)$  [M Schaeper & N Damaschke 2017].

$$c_k(t) = FT\{i(x-vt)\}_k \quad 3.4.2$$

The displacement law explains the movement of the intensity distribution of a time-dependent complex Fourier coefficient  $c_k(t)$  of spatial filter signal  $s(t)$  in the spectral domain.

$$FT\{i(x-vt)\} = FT\{i(x)\}e^{-jkvt}$$

3.4.3

For a moving intensity distribution, an increase in the phase of the spatial filter signal's Fourier coefficients is observed, indicating the amount of displacement in the respective harmonic part of the intensity distribution, and the amplitude indicates the amount of the respective spatial frequency in the intensity distribution.

It is essential to estimate the grating period ( $g_p$ ) or the spatial frequency ( $\mu = 1/g_p$ ) of the grating function because the output of the spatial filter represents the information of the structure with similar spatial frequencies in the image.

A description of how to choose the grating period using Fourier analysis is presented in M Schaeper & N Damaschke 2017. A 1D Fourier analysis along two axes of the image reveals the amplitude of the spatial frequencies along both directions. The dominant spatial frequencies produce a peak in the amplitude of the Fourier coefficients. However, it is also important to consider a higher Fourier coefficient to increase accuracy in phase value related to the structure. Later, the grating period is calculated as the ratio of the sampling frequency or the total number of pixels ( $n$ ) along the respective axis and the selected Fourier coefficient ( $m_0$ ).

$$g_p = \frac{n}{m_0}$$

3.4.4

To understand the spatial frequencies of NLC, roughly 50 images were manually identified with different NLC structures. Using the template and surface similarity parameter lower atmospheric clouds were masked. Later, Fourier coefficients for regions of 512x512 pixels of all the images excluding masked regions were calculated. The sum of all these coefficients shows cumulative dominant spatial frequency range. The resulting magnitude of the coefficients is shown in Figure 3.4. The increase in

magnitude for higher Fourier coefficients is typical due to the structures of the NLC. A trade-off between higher magnitude and higher Fourier coefficient is explained in M Schaeper & N Damaschke 2017. The coefficient  $m_0 = 23$  was chosen for the further analysis.

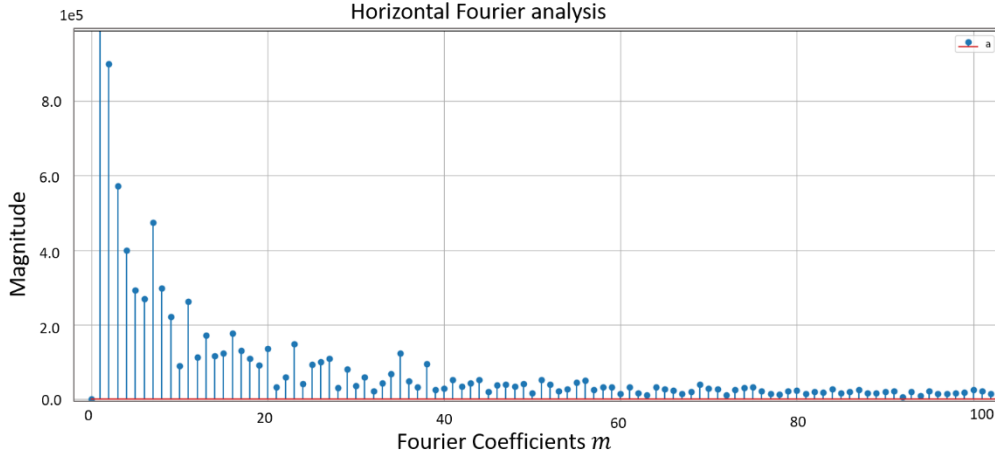


Figure 3.4: Fourier coefficients along the x-axis. Fourier coefficient  $m_0 = 23$  is considered for the desired grating period.

### 3.5 Detecting structural movements in the Sky

The lower atmosphere clouds in an image are masked by comparing the surface similarity between the test image with the relevant portion of the template as described in section 3.2. Weighting the resulting image with a complex grating function generates a complex spatial filter signal ( $s(t)$ ) [Equation 3.4.1]. The presence of the moving NLC structure (matching harmonic part with the respective grating period) generates a strong signal (high amplitude of the respective Fourier coefficient) from the product of  $s(t+1)$  and the conjugate of  $s(t)$ . The regions of the image with clear sky generate a noisy signal due to the absence of any moving structure. Calculating moving average over small areas reduces the amplitude of the noise, and a threshold amplitude of the signal ( $S$ ) can be used to mask the noise in the image to represent NLC:

$$S = s(t) * s(t+1) = Ae^{j(\phi_t - \phi_{t+1})}$$

Weighting the 1D grating function along both directions results in detection of 2D movement of NLC. The sum of both the signals improves the detection of NLC. It is worthy to note that in case the lower atmosphere clouds or stars are not entirely masked, their edges generate a high amplitude spatial filter signal.

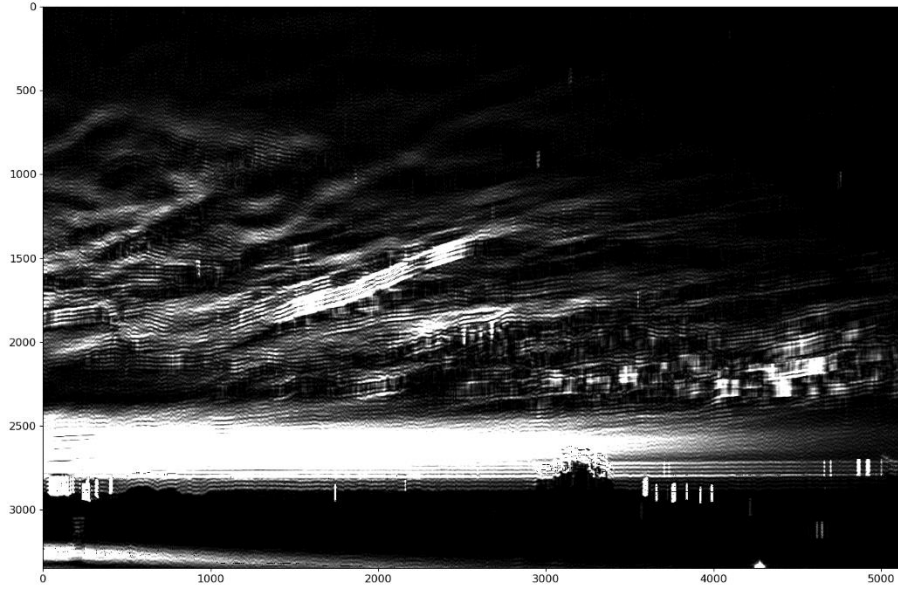


Figure 3.5: The amplitude ( $A$ ) of the signal ( $S$ ) for two images from Kühlungsborn on July 10<sup>th</sup>, 2015 (21:09:53 and 21:10:33 UT). The gray scale is proportional to  $S$  and ranges from 0 to  $2.5e^8$ . A minimum threshold amplitude  $A = 400$  is used to mask the image. The bright regions of the image represent the presence of NLC.

## 4 Localization of NLC

### 4.1 Pinhole Camera model

Pinhole camera model approximates the camera projection of 3D world to the 2D image plane. The pinhole camera can be visualised as a closed box [Figure 4.1] into which light passes through a small hole and projects an image on a photosensitive surface. The pinhole camera model explains the relation between the coordinates of the projected image and world coordinates [Gang Xu and Zhengyou Zhang 1996, Bernd Jähne 1997, David A. Forsyth and Jean Ponce 2003]

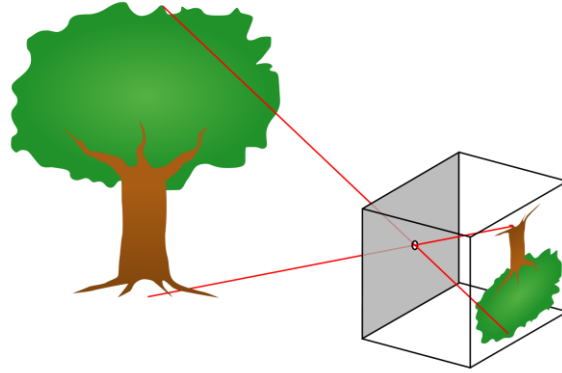


Figure 4.1: Simple illustration of a pinhole camera model. The light from outside world enters a closed box through an infinitesimally small hole and projects an inverted image on the photosensitive wall.

Figure 4.2 shows the construction of the image for the pinhole camera model. Consider an origin ( $O$ ) of a 3D orthogonal coordinate system at the pinhole or the aperture of the camera such that the optical axis is along the positive  $Z$  direction and the  $XY$  plane is the principal plane of the camera. The plane on which the image is projected is parallel to the principal plane, the centre of the image plane or the principal point ( $i$ ) is at a distance equal to the focal length ( $f$ ) of the camera from the origin ( $O$ ) along the negative direction of the principal axis.

A point  $P(X,Y,Z)$  in 3D world coordinate system is projected on to the image plane at  $p(x,y)$ . The point  $p(x,y)$  is the intersection of the image plane with the line joining



origin ( $O$ ) and point  $P(X,Y,Z)$ . All the points on the intersecting line ( $Pp$ ) are projected at a point  $p(x,y)$  on the image plane, thus losing the depth information of the 3D world.

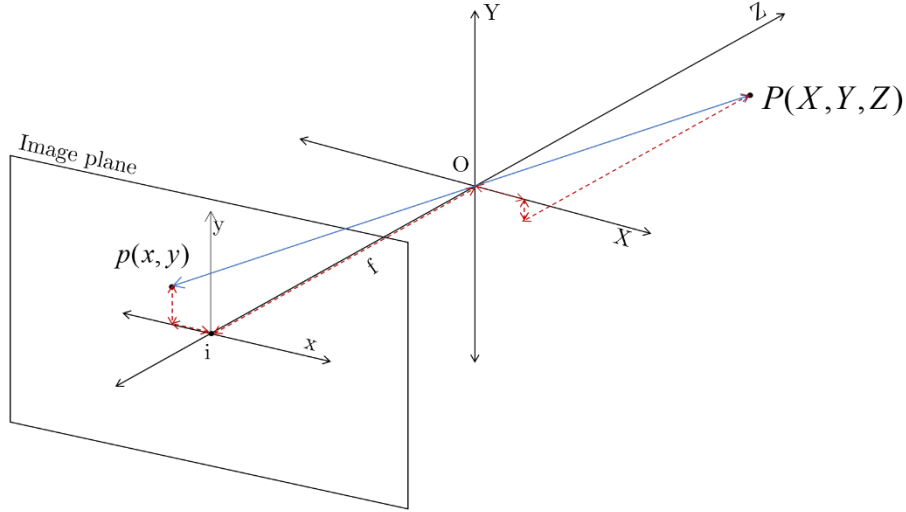


Figure 4.2: The 3D geometry of a pinhole camera model depicting the projection of global point  $P$  on to the image plane at point  $p$ .

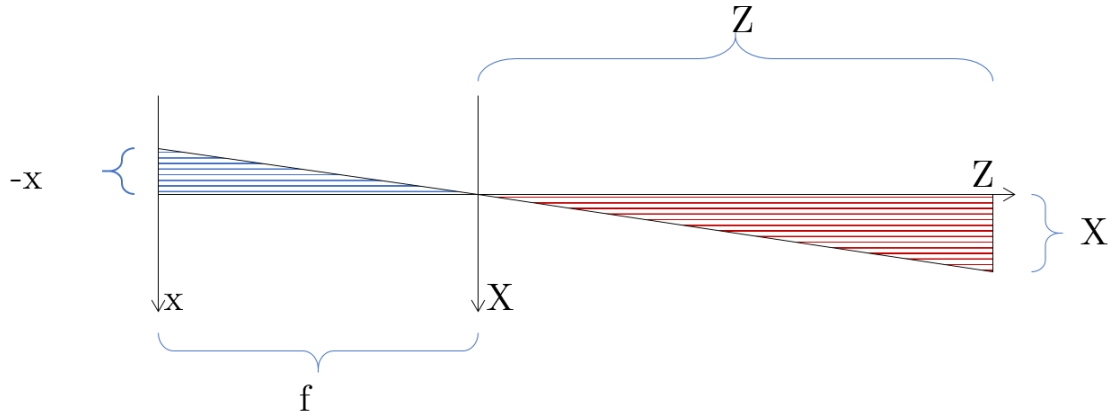


Figure 4.3: Projection along  $XZ$  plane of the pinhole camera model. The red shaded region is the outside world, and the blue shaded region is inside pinhole camera.

From the  $XZ$  plane shown in Figure 4.3, the relation between  $x$  and  $X$  can be formulated using the property of similar triangles, that is, the ratios of legs of two similar triangles are equal.

$$-\frac{x}{f} = \frac{x}{z} \Rightarrow x = -\frac{f}{z} X$$

Similarly, the relationship between  $y$  and  $Y$  can be formulated.

$$y = -\frac{f}{z}Y$$

4.1.2

The projection of the observed scene is inverted along both axes; this can be corrected by  $180^\circ$  rotation of the image plane. The projection of the object on to the image plane depends on the relative position of the camera and the object and is defined by perspective projection. The projected size of the objects on the image plane depends on the distance of the object from the camera, the projected size of an object becomes smaller as the distance from the object increases, and the size of the image depends on the focal length. The missing depth information of the 3D world can be reconstructed by using another camera observing the same object; this method is called Stereoscopy.

## 4.2 Stereoscopy depth measurement

Using the disparity in a pair of picture observing a scene from two distinct viewpoints, Charles Wheatstone in 1838 invented stereoscopic viewing devices for depth perception of the observed scene. In 1896 O Jesse published measurements of the altitude of NLC based on stereoscopic observations. The same idea is implemented in computer vision to measure the distance to an object of interest in a digital image from the image plane [Juber A Sheikh & M A Joshi 2016, Jernej Mrovlje & Damir Vrancic 2008].

Figure 4.4 illustrates a simple and ideal camera arrangement to capture a stereoscopic image pair. Two cameras ( $C_1$ ) and ( $C_2$ ) with the parallel principal axis, observing a point  $P(X,Y,Z)$  from a coplanar principal plane with zero deviation along the y-axis and are separated by a distance ( $d$ ) along x-axis. With the known focal length ( $f$ ), the separation ( $d$ ) of the cameras and the disparity between the projected positions ( $p_1'$ ) and ( $p_2'$ ) of the point ( $P$ ) in the image plane [Figure 4.5] of both cameras, the distance to the point ( $P$ ) from the baseline of the cameras can be calculated using the pinhole camera model.

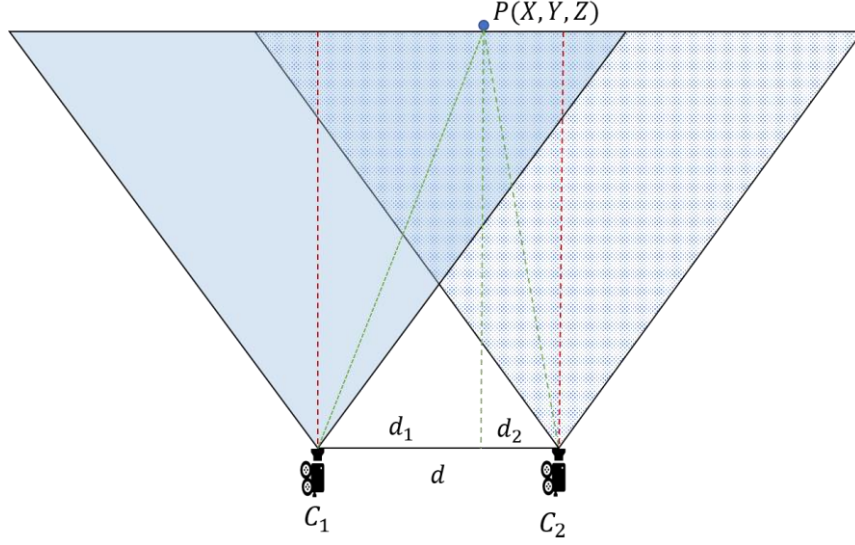


Figure 4.4: Ideal alignment of two cameras separated by a distance ( $d$ ) observing a point ( $P$ ) in the 3D world. The field of view is indicated by shaded areas. Red lines represent the optical axis of the camera.

Figure 4.5 shows the simplified layout geometry with the projection of a point ( $P$ ) in the image plane of both cameras. The disparity ( $D$ ) between the projections of the point ( $P$ ) in two images is  $x_2 - x_1$ . The distance ( $R$ ) to the point ( $P$ ) can be derived as follows.

$$D = x_2 - x_1 \Rightarrow f \left( \frac{x_2}{f} + \frac{x_1}{f} \right); \text{ Here } x_1 \text{ is negative} \quad 4.2.1$$

From the properties of similar triangles.

$$D = f \left( \frac{d_2}{R} + \frac{d_1}{R} \right) \Rightarrow \frac{f}{R} (d_2 + d_1) \quad 4.2.2$$

Solving the previous Equation for  $R$  we get:

$$R = \frac{f \cdot d}{D} \quad 4.2.3$$

The range to  $P$  can be calculated using the focal length, the length of the baseline between the cameras ( $d$ ) and the disparity ( $D$ ) of the imaging point.

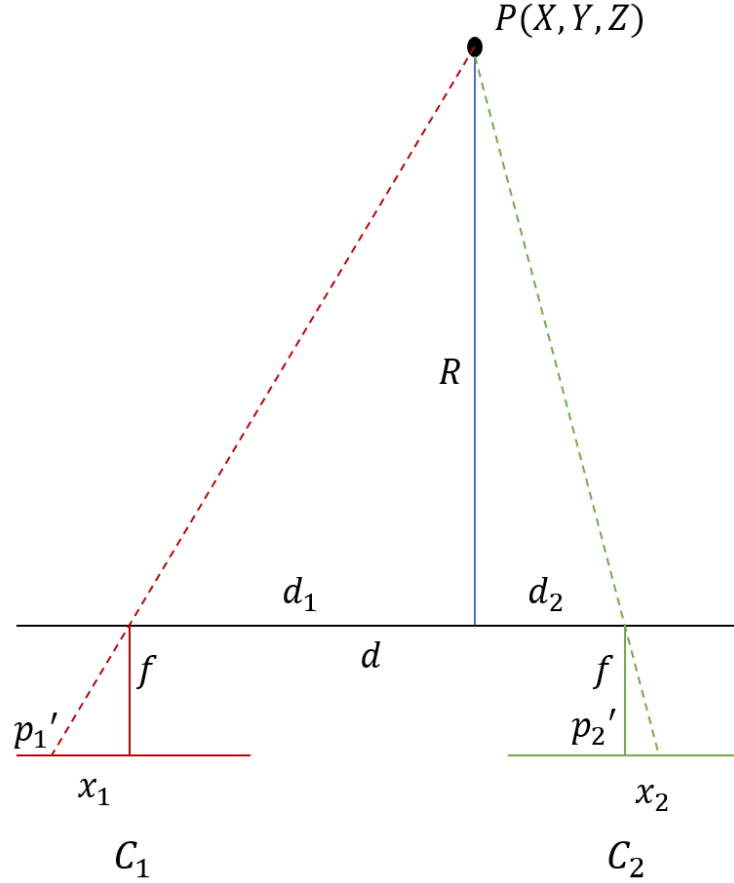


Figure 4.5: Simple layout of the projection of point  $P$  on to the image plane of both cameras using pinhole camera model.

### 4.3 Homogeneous Coordinate Transformation

Homogeneous coordinates or projective coordinates are the systems of coordinates used in projective geometry as cartesian coordinates used in Euclidean geometry. The number of coordinates required to represent a point in the homogeneous coordinate system is one more than the number of dimensions of the space. A point  $E(x, y, z)$  in Euclidean space can be represented in a homogeneous coordinate system using a non zero scalar factor  $k$  as  $H(\frac{x}{k}, \frac{y}{k}, \frac{z}{k}, k)$ . If  $k=0$ , a point at infinity can be represented using finite coordinates [Yan-Bin Jia 2017, Stöcker H 2007, Briot S & Khalil W 2015].

Homogeneous coordinate transformations are widely used in computer graphics and robotics to determine the relationship between the points and the vectors of different frames of reference. Calculations of projections and perspective transformations can be

performed efficiently by using homogeneous coordinate transformations. A transformation of a projective space is given by  $M : P^3 \rightarrow P^3$ . Where  $M$  is the 4x4 homogeneous transformation matrix and  $m_{ij} \in \mathbb{R}$ . If  $m_{11} = m_{22} = m_{33} = 1$  and  $m_{44} \neq 0$  then  $M$  can be used for affine transformations (translation, scaling and rotation) of 3D space.

$$\begin{bmatrix} x \\ y \\ z \\ w \end{bmatrix} \xrightarrow{M} \begin{bmatrix} m_{11} & m_{12} & m_{13} & m_{14} \\ m_{21} & m_{22} & m_{23} & m_{24} \\ m_{31} & m_{32} & m_{33} & m_{34} \\ m_{41} & m_{42} & m_{43} & m_{44} \end{bmatrix} \begin{bmatrix} x \\ y \\ z \\ w \end{bmatrix} \quad 4.3.1$$

A homogeneous transformation matrix for translation by a unit of  $a$ ,  $b$ , and  $c$  along  $x$ ,  $y$ , and  $z$  direction respectively [Figure 4.6] is denoted as  $Trans(a,b,c)$ .

$$Trans(a,b,c) = \begin{bmatrix} 1 & 0 & 0 & a \\ 0 & 1 & 0 & b \\ 0 & 0 & 1 & c \\ 0 & 0 & 0 & 1 \end{bmatrix} \quad 4.3.2$$

Using this transformation matrix ( $M$ ) any point  $P'(x,y,z,1)^T$  in a 3D translated space ( $C'$ ) can be represented as ( $P$ ) in the original/initial 3D space ( $C$ ) by multiplying the point with the translation matrix  $Trans(a,b,c)$ .

$$\begin{aligned} P &= Trans(a,b,c)P' \\ P &= \begin{bmatrix} 1 & 0 & 0 & a \\ 0 & 1 & 0 & b \\ 0 & 0 & 1 & c \\ 0 & 0 & 0 & 1 \end{bmatrix} \begin{bmatrix} x \\ y \\ z \\ 1 \end{bmatrix} = \begin{bmatrix} x+a \\ y+b \\ z+c \\ 1 \end{bmatrix} \\ P &= (x+a, y+b, z+c, 1)^T \end{aligned} \quad 4.3.3$$

The inverse of the translation matrix ( $M$ ) maps any point in  $C$  to  $C'$ .

$$P' = Trans(a,b,c)^{-1}P \quad 4.3.4$$

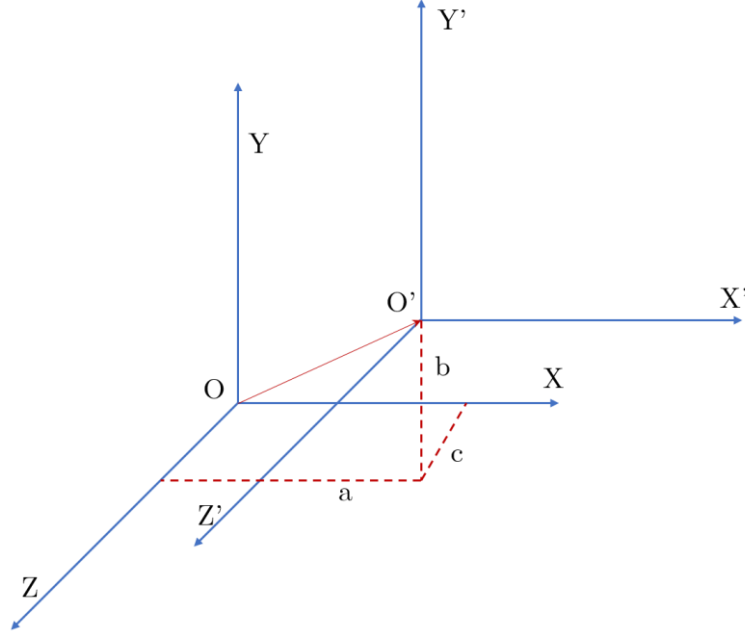


Figure 4.6: Representation of pure coordinate translation from origin  $O$  to  $O'$  by an amount of  $a$ ,  $b$ , and  $c$  along  $X$ ,  $Y$ , and  $Z$  axes respectively.

The homogeneous transformation matrix for scaling about an origin by a factor of

$\left( \frac{s_x}{s_w}, \frac{s_y}{s_w}, \frac{s_z}{s_w} \right)$  over  $x$ ,  $y$ , and the  $z$  axis is denoted as  $Scale(s_x, s_y, s_z, s_w)$ .

$$Scale(s_x, s_y, s_z, s_w) = \begin{bmatrix} s_x & 0 & 0 & 0 \\ 0 & s_y & 0 & 0 \\ 0 & 0 & s_z & 0 \\ 0 & 0 & 0 & s_w \end{bmatrix}$$

4.3.5

Using this transformation matrix ( $M$ ) any point  $P'(x, y, z, 1)^T$  in a 3D scaled space ( $C'$ ) can be represented as  $P$  in the original/initial 3D space ( $C$ ) by multiplying the point with the scaling transformation matrix  $Scale(s_x, s_y, s_z, 1)$ , where  $s_w = 1$ .

$$P = \begin{bmatrix} s_x & 0 & 0 & 0 \\ 0 & s_y & 0 & 0 \\ 0 & 0 & s_z & 0 \\ 0 & 0 & 0 & 1 \end{bmatrix} \begin{bmatrix} x \\ y \\ z \\ 1 \end{bmatrix} = \begin{bmatrix} x \cdot s_x \\ y \cdot s_y \\ z \cdot s_z \\ 1 \end{bmatrix}$$

4.3.6

A rotational transformation matrix of an angle  $(\theta)$  around  $x$ ,  $y$ , and  $z$  axes are denoted as  $Rot(x, \theta)$ ,  $Rot(y, \theta)$  and  $Rot(z, \theta)$  respectively and the direction of rotation is given by right hand thumb rule.

$$Rot(x, \theta) = \begin{bmatrix} 1 & 0 & 0 & 0 \\ 0 & \cos \theta & -\sin \theta & 0 \\ 0 & \sin \theta & \cos \theta & 0 \\ 0 & 0 & 0 & 1 \end{bmatrix}$$

4.3.7

$$Rot(y, \theta) = \begin{bmatrix} \cos \theta & 0 & \sin \theta & 0 \\ 0 & 1 & 0 & 0 \\ -\sin \theta & 0 & \cos \theta & 0 \\ 0 & 0 & 0 & 1 \end{bmatrix}$$

4.3.8

$$Rot(z, \theta) = \begin{bmatrix} \cos \theta & -\sin \theta & 0 & 0 \\ \sin \theta & \cos \theta & 0 & 0 \\ 0 & 0 & 1 & 0 \\ 0 & 0 & 0 & 1 \end{bmatrix}$$

4.3.9

By sequential multiplication of these transformational matrices, transformation to any frame of reference is possible. The mapping between any number of frames of reference can be represented simply by one transformation matrix as the product of all the transformation matrices. In Figure 4.7 a transformation matrix mapping from the frame  $(\mathcal{F}_0)$  to frame  $(\mathcal{F}_1)$  is represented as  ${}^0T_1$  and from the frame  $(\mathcal{F}_1)$  to frame  $(\mathcal{F}_2)$  is represented as  ${}^1T_2$ . The  $k^{th}$  transformation matrices mapping from  $\mathcal{F}_0$  to  $\mathcal{F}_k$  can be represented as  ${}^0T_1 \times {}^1T_2 \times {}^2T_3 \times \dots \times {}^{k-1}T_k = {}^0T_k$ . Note that the sequence of multiplying transformation matrices is very important, a different order of multiplication leads to a different frame of reference.

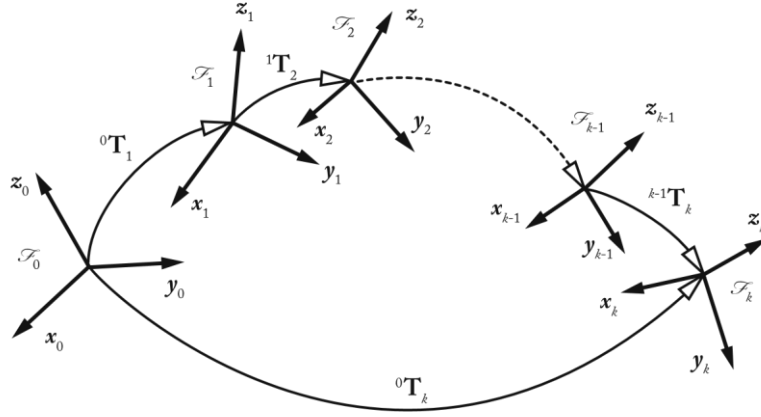


Figure 4.7: Transformation of the frame of reference from  $\mathcal{F}_0$  to  $\mathcal{F}_k$  by multiple translation and rotations [Briot S & khalil W 2015].

## 4.4 NLC range calculation

### 4.4.1 Coordinate system

Different models of Earth are available for use in geodesy and navigation. In this thesis work, World Geodetic System 1984 [WGS84] is used. WGS84 describes three standard surfaces based on topography, standard oblate spheroidal reference and a gravitational equipotential surface that defines average sea level. The coordinate origin of WGS84 is at Earth's centre of mass. A spheroid is a quadratic surface obtained by rotation of an ellipse, the rotation over minor axis results in an oblate/flattened spheroid. The Earth spheroidal surface is defined with two parameters, flattening  $f = (a - b)/a$  and the first eccentricity squared  $e^2 = 2f - f^2$ , where  $a = 6,378,137$  m is the length of semi-major axis, and  $b = 6,356,752.3142$  m is the length of the semi-minor axis.



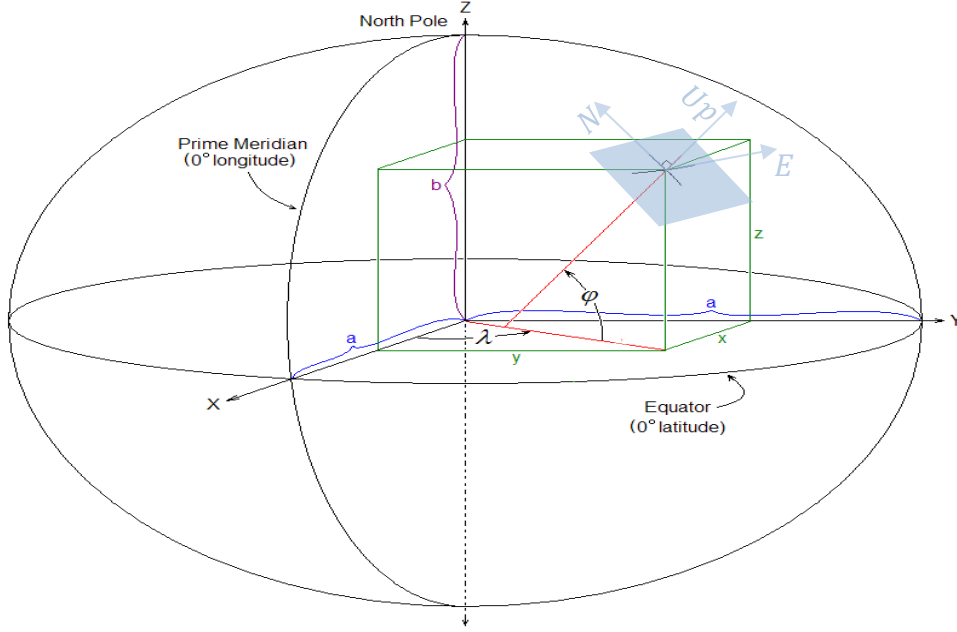


Figure 4.8: An oblate surface model of Earth. Earth Centred Earth Fixed coordinates in relation to latitude and longitude. The origin is located at the centre of mass of earth.  $a$  is semi-major axis,  $b$  is semi-minor axis,  $\varphi$  is latitude,  $\lambda$  is longitude, X-Y-Z is ECEF coordinate system, and E-Up-N is local ENU coordinate system.

#### 4.4.2 Converting pixel position to azimuth and elevation

After detecting the NLC regions in an image from Kühlungsborn, a selected pixel position in an image captured from Kühlungsborn is converted to the approximate pixel position in an image captured from IOW. For this, the precise position and pointing of the camera, as well as the camera field of view and projection type, are needed. The actual values were taken from [Schäfer 2016].

The camera view, that is, the azimuth and elevation of the centre pixel and the rotation of the sensor axis of the camera with respect to the horizon are estimated by comparing star traces of a selected imaging period with those calculated from a star almanac (SKY 2000 Master Catalogue, version 4) using PyEphem and Astropy library. The comparison to star traces also gives the horizontal and vertical field (resolution of the camera) of view and the projection type. The azimuth and elevation of a selected NLC pixel in an image are then calculated using the WCS function of the Astropy python library with the known parameters of the camera. The function requires the camera

view, the resolution, and the lens projection. The function also considers the atmospheric refraction for calculating the elevation angle.

#### 4.4.3 Estimating Latitude, Longitude and Altitude using Homogeneous Coordinate Transformations

The geodetic coordinates (latitude, longitude and altitude) are based on the Earth Centred Earth Fixed (ECEF) coordinate system, where the origin of this coordinate system is at the centre of mass of the Earth. The  $x$ -axis points towards the Prime Meridian,  $y$ -axis points towards the East and  $z$ -axis passes through the North pole. A local coordinate system of an observer is defined as East-North-Up (ENU). The East-axis is tangent to the local meridian, North-axis is tangent to local latitude pointing towards true North and Up-axis is normal to the local tangent plane and point away from the centre of Earth (the normal to the local tangent plane might not pass through the centre of the Earth) see Figure 4.8.

Nomenclature:

- $h_K, h_I, h_{NLC}$  GPS height/height above ellipsoid of Kühlungsborn, IOW cameras and NLC
- $\varphi_K, \lambda_K; \varphi_I, \lambda_I$  Latitude and Longitude of Kühlungsborn and IOW cameras.
- $\varphi_{NLC}, \lambda_{NLC}$  Latitude and Longitude of the target NLC point.
- Normal  $N_\varphi = \frac{a}{\sqrt{1-e^2 \sin^2 \varphi}}$

Coordinates of Kühlungsborn with respect to ECEF.

$$K_{ECEF} = \begin{bmatrix} x_K \\ y_K \\ z_K \\ 1 \end{bmatrix} = \begin{bmatrix} (N_{\varphi_K} + h_K) \cos \varphi_K \cos \lambda_K \\ (N_{\varphi_K} + h_K) \cos \varphi_K \sin \lambda_K \\ (N_{\varphi_K} (1-e^2) + h_K) \sin \lambda_K \\ 1 \end{bmatrix}$$

4.4.1

Coordinates of IOW with respect to ECEF.

$$I_{EFEC} = \begin{bmatrix} x_I \\ y_I \\ z_I \\ 1 \end{bmatrix} = \begin{bmatrix} (N_{\varphi_I} + h_I) \cos \varphi_I \cos \lambda_I \\ (N_{\varphi_I} + h_I) \cos \varphi_I \sin \lambda_I \\ (N_{\varphi_I} (1 - e^2) + h_I) \sin \lambda_I \\ 1 \end{bmatrix}$$

4.4.2

Coordinates of NLC with respect to ECEF.

$$NLC_{EFEC} = \begin{bmatrix} x_{NLC} \\ y_{NLC} \\ z_{NLC} \\ 1 \end{bmatrix} = \begin{bmatrix} (N_{\varphi_{NLC}} + h_{NLC}) \cos \varphi_{NLC} \cos \lambda_{NLC} \\ (N_{\varphi_{NLC}} + h_{NLC}) \cos \varphi_{NLC} \sin \lambda_{NLC} \\ (N_{\varphi_{NLC}} (1 - e^2) + h_{NLC}) \sin \lambda_{NLC} \\ 1 \end{bmatrix}$$

4.4.3

The Transformation matrix to transform any ENU coordinate point with respect to K hlungsborn to ECEF coordinate point is formed by first translating the coordinate system from the centre of the Earth to  $K_{EFEC}$  and later by rotating over  $Y$ -axis (latitude) and over  $Z$ -axis (longitude).

$$K_{EFEC}^{ENU} = \begin{bmatrix} \cos \varphi_K & -\sin \varphi_K & 0 & 0 \\ \sin \varphi_K & \cos \varphi_K & 0 & 0 \\ 0 & 0 & 1 & 0 \\ 0 & 0 & 0 & 1 \end{bmatrix} \begin{bmatrix} \cos(90 - \lambda_K) & 0 & \sin(90 - \lambda_K) & 0 \\ 0 & 1 & 0 & 0 \\ -\sin(90 - \lambda_K) & 0 & \cos(90 - \lambda_K) & 0 \\ 0 & 0 & 0 & 1 \end{bmatrix} \begin{bmatrix} 1 & 0 & 0 & x_K \\ 0 & 1 & 0 & y_K \\ 0 & 0 & 1 & z_K \\ 0 & 0 & 0 & 1 \end{bmatrix}$$

$Rot(Z)$   $Rot(Y)$   $Trans(x_K, y_K, z_K)$

4.4.4

NLC coordinates with respect to ENU K hlungsborn

$$K_{NLC} = \begin{bmatrix} E_{NLC}^K \\ N_{NLC}^K \\ U_{NLC}^K \\ 1 \end{bmatrix} = K_{ENU}^{EFEC} \begin{bmatrix} x_{NLC} \\ y_{NLC} \\ z_{NLC} \\ 1 \end{bmatrix}; \text{ where } K_{EFEC}^{ENU}^{-1} = K_{ENU}^{EFEC}$$

4.4.5

The azimuth and elevation of the selected pixel in an image is calculated as described in section 4.4.2. The local ENU coordinates of NLC with respect to K hlungsborn,  $E_{NLC}^K$  and  $N_{NLC}^K$  are calculated from azimuth ( $\alpha$ ) and elevation ( $\beta$ ) using below

equations. As the slant range ( $r$ ) to the NLC is not known, it is estimated by assuming that the NLC is at a given altitude.

$$\tan \alpha = \frac{E_{NLC}^K}{N_{NLC}^K} ; \tan \beta = \frac{U_{NLC}^K}{\sqrt{E_{NLC}^{K^2} + N_{NLC}^{K^2}}}$$

4.4.6

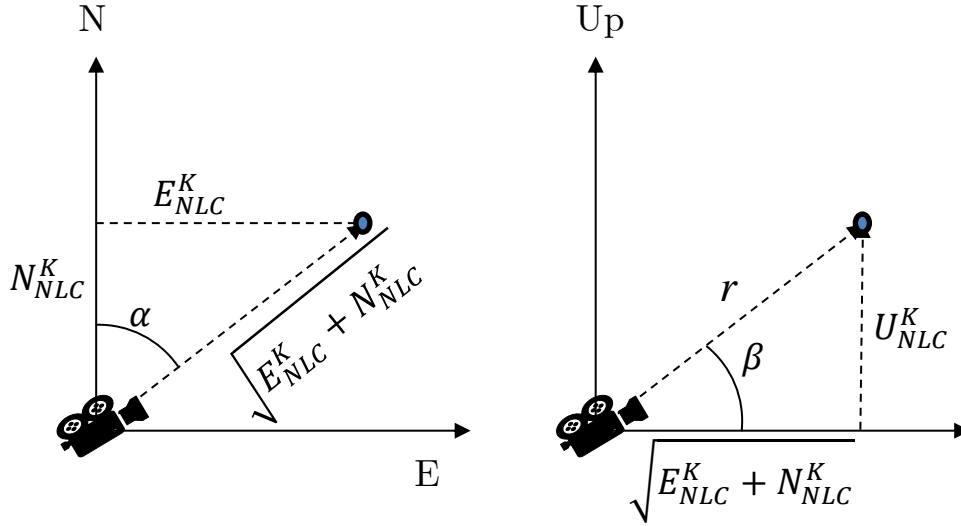


Figure 4.9 Left: Top view of local coordinate system ENU. Right: Sided view of ENU. The blue point indicates the position of the NLC

By solving  $K_{NLC} = K_{ENU}^{ECEF}(NLC_{EFEC})$ , we get  $\varphi_{NLC}$  and  $\lambda_{NLC}$ . The conversion of the geodetic to ECEF coordinates is easily performed as outlined above. However, the conversion of ECEF to geodetic coordinates is more complicated due to the deviation of the Earth's surface from a sphere. Several algorithms were developed, e.g., [Vermeille 2002]. For solving  $K_{NLC}$  for a given  $h_{NLC}$  a numerical iterative solver is used. The solver converts azimuth, elevation and slant range to geodetic coordinates (latitude, longitude and altitude) using the PyMap3d python library and iterates to find the slant range that results in the prescribed NLC altitude. With the known latitude, longitude and altitude of the selected pixel in an image from K hlungsborn, an approximate azimuth and elevation are calculated from the above-mentioned coordinate transformation, and then the pixel in the image from IOW representing the same location is estimated using WCS function from Astropy python library same as mentioned in section 4.4.2. Starting with this approximate pair of pixels the range from the camera baseline is calculated

in the following section. This range then allows to calculate the correct geodetic coordinates of the NLC.

#### 4.4.4 Range from the camera's baseline

To calculate the range of the structure at the approximated pixel using stereoscopy depth measurement technique, the disparity of the structure with respect to a reference point in both the image planes is needed. A star can be considered as a reference point for both the images since the starlight coming from a very far distance can be assumed as parallel to both the cameras. By considering a star nearby to the selected pixel, the error due to atmospheric refraction can be minimised as the light is refracted by approximately an equal factor for both NLC and the star. The disparity along both axes  $x$  and  $y$  is given by the difference of the number of pixels between the two-selected pixel and a nearby star. To correct the disparity calculated using approximated pixel positions the spatial filter signal is used.

The spatial filter signal is generated by integrating over an area around the approximated pixel. The width of the integration area is 10 pixels, and the length is five times the estimated grating period ( $g_p$ ) of the NLC structure. The Position of the structure in the selected area is calculated in multiple steps (see Figure 4.10). First, a grating function with a grating period ( $gp_1$ ) equal to the length of the integration area is weighed over the selected area, the phase ( $\phi_1$ ) is calculated from the spatial filter signal. The phase ( $\phi_1$ ) gives an approximate position ( $x_1$ ) of the structure. The same process is repeated with a grating period equal to half of the previous value, and the phase ( $\phi_2$ ) is calculated. For the position of the structure, ( $x_2$ ) is calculated from Equation 4.4.7 where  $n$  is the floor division of  $x_1$  and  $gp_1$  (Floor division: Division that results in the whole number adjusted to left on the positive number line and right on the negative number line).

$$x_2 = \frac{2n\pi + \phi_2}{2\pi} gp_2$$

4.4.7

Repeating this process gives the more precise position of the structure. However, by decreasing the grating period, the spatial filter generates signals representing higher

Fourier coefficients in the spectral domain, but may not represent the intended structure. Furthermore, if there are more than one structures in the selected area than the phase output may not represent the correct position.

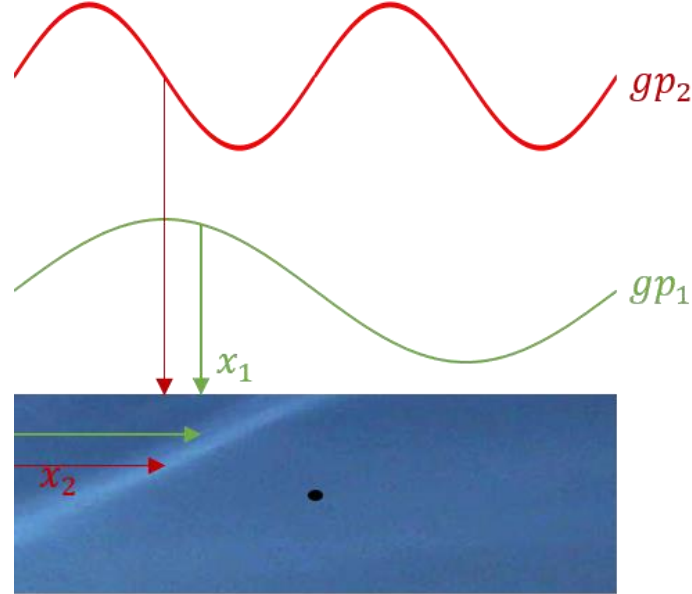


Figure 4.10: Searching for the NLC structure in an integration area selected around the initially approximated pixel. The black dot indicates the initial pixel position. Green colour indicates first step and the red colour indicates the second step.

By implementing this process to both the images from Kühlungsborn and IOW, an accurate disparity between the similar structure can be identified in reference to a nearby star. The NLC range, normal to the baseline plane is then calculated as described in section 4.2. With the resulting range and already calculated azimuth and elevation, the altitude of the NLC can be calculated by PyMap3d python library.

The position of the structure in the selected area can also be calculated by using bisection search method and the formula  $x = \frac{\varphi}{2\pi} g_p$ , where  $x$  is the distance from the beginning of the integration area. The first approximate position  $x_1$  of the structure is calculated using the first step of the previous method, for the next step, a smaller integration area half in length of the previous area is selected around the new position and the grating period is always equal to the length of the selected area. This method leads to errors when repeating more than two to three steps as the selected area may not host the structure anymore. With this method the error caused by the presence of

---

more than one structure can be eliminated, if the following integration area does not host the structure, then the resulting amplitude of the spatial filter signal is zero, and the structure can be searched in the remaining area.

## 5 Summary & Outlook

### 5.1 Summary

Previous studies of NLC images briefly describe the plausible conditions for observation of NLC by calculating the NLC observability rate for different solar elevation angles, days from and to solstice and latitude of observation location [Baumgarten G 2009, Gadsden M & Schröder W 1989]. In recent bachelor thesis work [Schmidt 2013], KNN algorithm was developed to automatically detect the NLC regions of an image purely depending on colour ratios. However, on further investigation, it turned out that using a more extensive set of sky observations requires additional NLC indicators.

In this thesis work, around 210,000 images were analysed, and sets of images of the clear sky, NLC and low altitude clouds were extracted. An algorithm based on compensation parameter ( $CP$ ) is developed to investigate the nonlinearity of the camera by observing the vertical intensity distribution of the sky.  $CP$  is then used to identify suitable camera settings to obtain consistent results. Furthermore, the templates of clear sky images were constructed using  $CP$ . By comparing these template images with test images based on a surface similarity parameter ( $SSP$ ) is described in section 3.2, and a threshold value is established to separate lower atmosphere clouds, i.e., dark clouds. The presence of NLC structures in these dark cloud-free images is detected by implementing spatial filtering techniques. The advantage of complex grating function (section 3.4) to detect the movements of a harmonic structure is used to identify the regions of an image with NLC (section 3.5).

The algorithms for the triangulation of the NLC altitude (stereoscopic measurement of depth) described by [Schäfer 2016] were revisited and discussed in section 4.4. An approximate altitude is used to coarsely find the structures in one camera view from the second camera view. The phase output from the spatial filter signal is used to identify exact pixel position of the similar structures from both the cameras. Based on the disparity of the structure in reference to a nearby star exact slant range is calculated and used to calculate the exact NLC altitude.



## 5.2 Outlook

Section 4.4 outlines the transformation of pixel coordinates to geodetic coordinates. These transformations allow mapping the images from camera view to horizontal scale at a fixed altitude above the Earth spheroid (worldview). Such mappings are used for example by Google Earth. Using triangulation of structures in a fully automated way allows to relax the assumption of a fixed NLC altitude, and the mapping can be done using the altitude calculated at multiple pixel pairs. Furthermore, the NLC identification can be applied to the mapped view. This allows the spatial filter to detect the properties of gravity waves, as the NLC structures are given by horizontal scales of the gravity wave. By analysing the orientation of the structures in the image, it is possible to optimise the grating function specific to the observed scene to obtain better results.

Applying these procedures to a more extensive dataset will allow to estimate uncertainties and identify the limitations of the current camera system. From the observations in sections 2.3 and 2.4, it is clear that the present camera system has some nonlinear characteristics due to which many images were not considered. Using a more sensitive and linear Multi-Spectral camera system could improve the NLC detection by vertical intensity distribution and colour ratios.

## References.

- Aizu Y & Asakura T 2006. Spatial Filtering Velocimetry Fundamentals and Applications. Berlin Springer
- Albrecht H E, Borzs M, Damaschke N & Tropea C 2003. Laser Doppler and Phase Doppler Measurement Techniques, Berlin Springer
- Ator J T 1963 Image velocity sensing with parallel slit reticles J. Opt. Soc. Am. 53 1325-31
- Bergeler S & Krambeer H 2004. Novel optical spatial filtering methods based on 2D photodetector arrays. Meas. Sci. Technol 15 1309-15
- Bernd Jähne 1997. Practical Handbook on Image Processing for Scientific Applications. CRC Press. ISBN 0-8493-8906-2.
- Briot S & khalil W 2015. Dynamics of Parallel Robots From Rigid Bodies to Flexible Elements. ISBN 978-3-319-19787-6
- Britta Schäfer Bachelor thesis 2016 Bestimmung von Höhe und horizontaler Struktur leuchtender Nachtwolken (NLC) aus Kamerabildern durch Triangulation
- Daniel Schmidt Bachelor thesis 2013 Automatische Erkennung von leuchtenden Nachtwolken in Kamerabeobachtungen
- David A. Forsyth & Jean Ponce 2003. Computer Vision, A Modern Approach. Prentice Hall. ISBN 0-12-379777-2.
- G. Baumgarten, M. Gerding, B. Kaifler, & N. Müller 2009. A Trans European Network of Cameras for Observation of Noctilucent Clouds From 37°N to 69°N
- Gang Xu & Zhengyou Zhang 1996. Epipolar geometry in Stereo, Motion and Object Recognition. Kluwer Academic Publishers. ISBN 0-7923-4199-6.
- Hosokawa S & Tomiyama A 2011. Spatial filter velocimetry based on time series particle images Exp. Fluids 52 1361-72
- J Craig 1989. Introduction to Robotics: Mechanics and Control. 2nd ed. Addison Wesley.
- Jernej Mrovlje & Damir Vrancic 2008. Distance measuring based on stereoscopic pictures. 9th International PhD Workshop on Systems and Control. Izola, Slovenia

- 
- Jesse O. 1896. *Astron. Nachrichten*, 140, 161
  - Juber A Sheikh & M A Joshi 2016. Stereo Images for Depth Measurement IEEE 978-1-5090-0774-5
  - M Schaeper & N Damaschke 2017. Fourier based layout for grating function structure in spatial filtering velocimetry. *Meas. Sci. Technol* 28 1361-6501
  - M Schaeper, I Menn, H Frank, N Damaschke 2008. Spatial filtering technique for measurement of 2C flow velocity. 14th Int Symp on Applications of Laser Techniques to Fluid Mechanics, Lisbon, Portugal
  - PyEphem. <http://rhodesmill.org/pyephem/#documentation>
  - PyMap3d. <https://github.com/scivision/pymap3d>
  - Raffel M, Willert C E, Wereley S T & Kompenhans J 2007. Particle Image Velocimetry, a Practical Guide, Berlin Springer.
  - Rapp M. & Thomas G E 2006. *J Atmos. Sol. Terr. Phys.*, 68, 715
  - Sakai Y, Uno T, Takagi J & Yamashita T 1995. Optical spatial filter sensor for ground speed *Opt. Rev* 2 65-7
  - Schaeper M 2014 *Mehrdimensionale Orsfiltertechnik*, Dordrecht Springer
  - Stöcker H 2007. *Taschenbuch mathematischer Formeln und moderner Verfahren*. Verlag Harri Deutsch. ISBN 978-3-8171-1811-3
  - Thomas G E, Olivero J J, Jensen E J, Schroeder, W., & Toon, O. B. 1989, *Nature*, 338, 490
  - Vermeille H H 2002. Direct Transformation from Geocentric to Geodetic Coordinates. *J. Geod.* 76 (8): 451–454. doi:10.1007/s00190-002-0273-6.
  - WGS84. [https://en.wikipedia.org/wiki/World\\_Geodetic\\_System](https://en.wikipedia.org/wiki/World_Geodetic_System)
  - Witt G. 1962. *Tellus*, 14, 1
  - World Coordinate System, Astropy. <http://docs.astropy.org/en/stable/wcs>
  - Yan-Bin Jia 2017. <http://web.cs.iastate.edu/~cs577/handouts/homogeneous-transform.pdf>
  - Zahn U. 2003. *EOS Transactions*, 84, 261

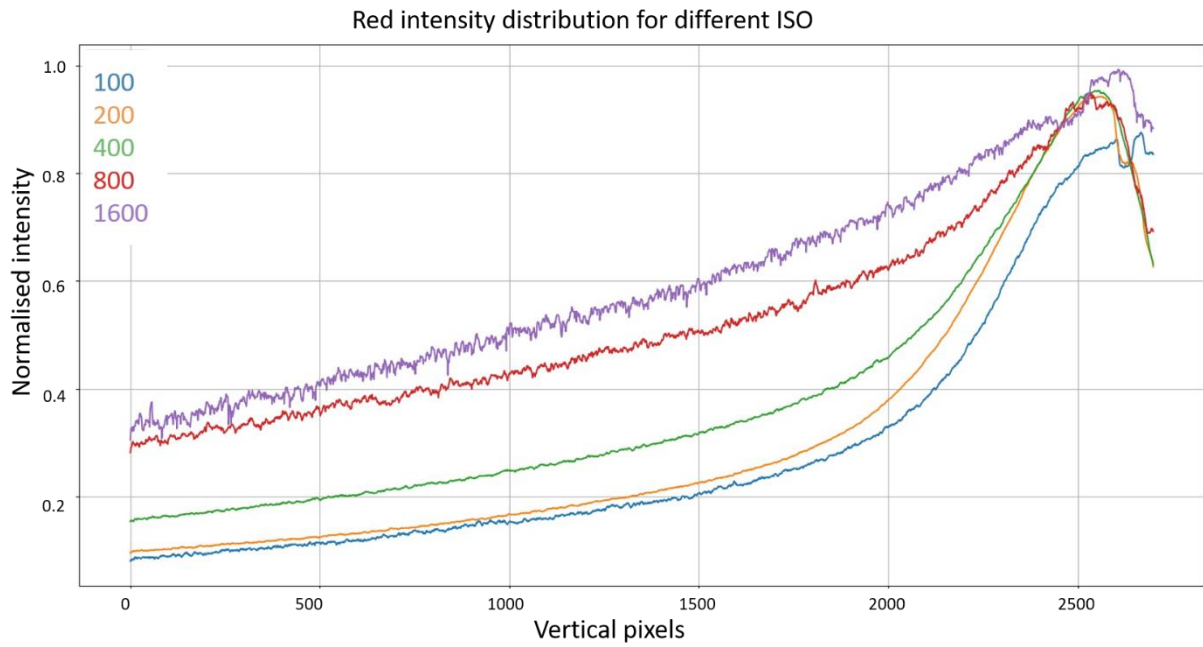
## Statutory declaration

I, Manoj Raman Kondabathula, declare that I have written this master thesis on my own and I have given all used references.

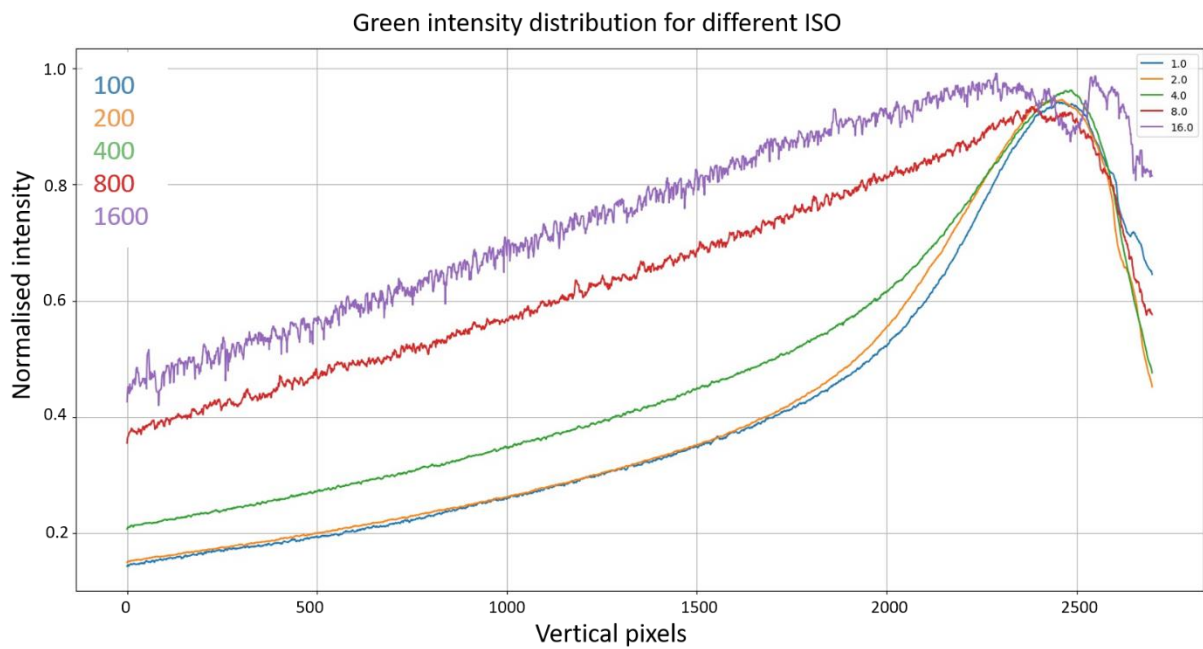
Rostock, 11.05.2018

Manoj Raman Kondabathula

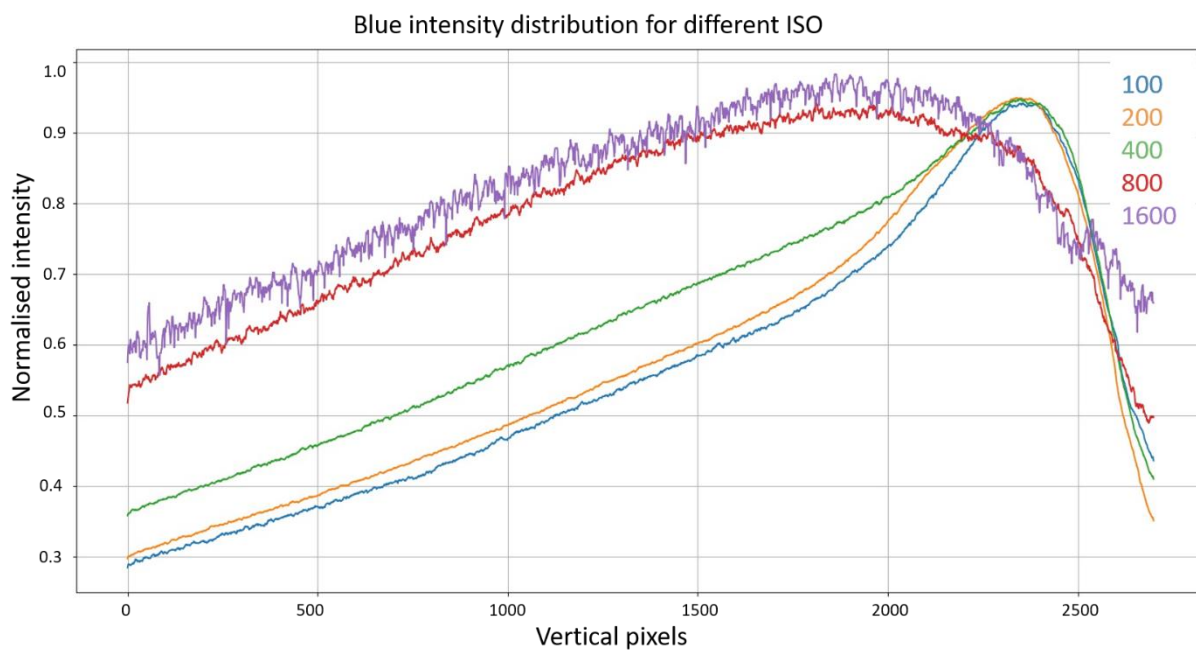
## Appendix A :



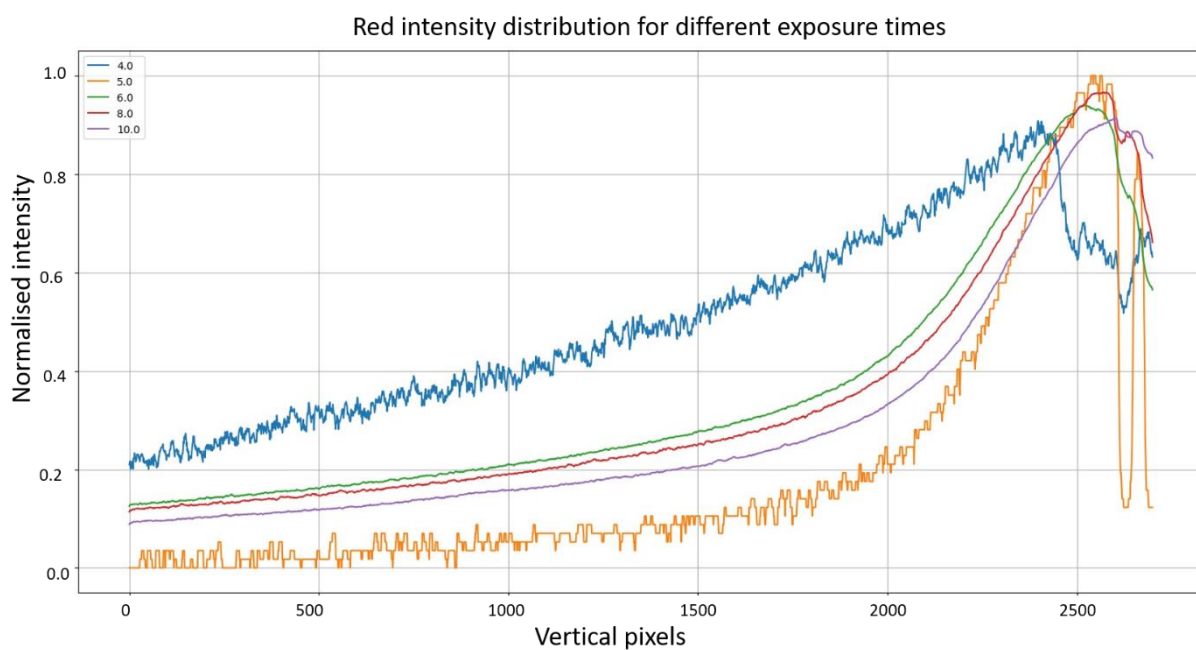
Normalised mean vertical red intensity distribution for images with different ISO settings



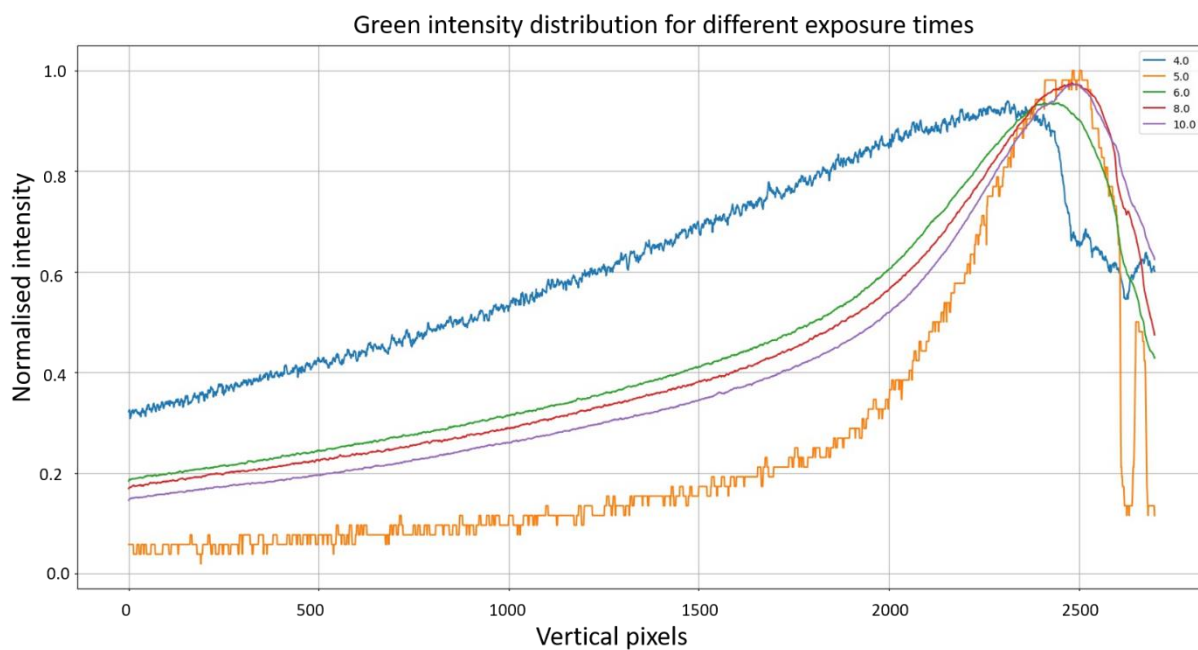
Normalised mean vertical green intensity distribution for images with different ISO settings



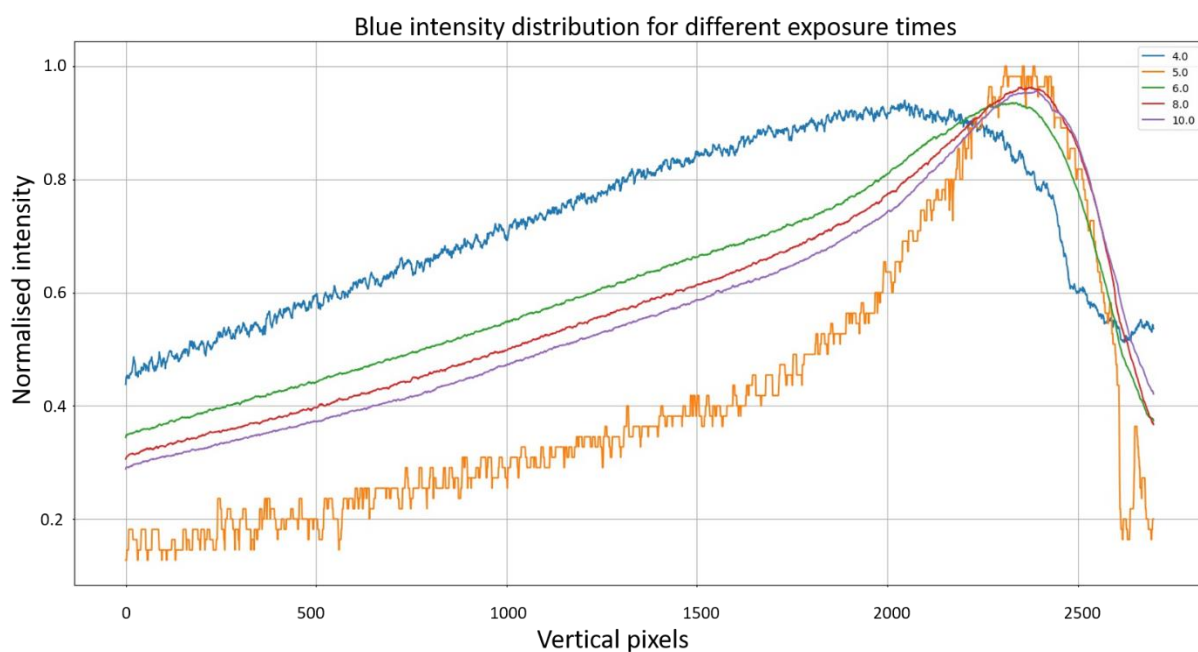
Normalised mean vertical blue intensity distribution for images with different ISO settings



Normalised mean vertical red intensity distribution for images with different exposure time settings



Normalised mean vertical green intensity distribution for images with different exposure time settings



Normalised mean vertical blue intensity distribution for images with different exposure time settings

## **A Note of Thanks**

While I put down the last words of my thesis, I recollect the memories of the wonderful journey I made. I feel honoured to be able to pursue post-graduation from the grand old University of Rostock and the quality education it imparted to me. I like to thank Dr Gerding for providing the much-needed opportunity and friendly support and Mr Söder for being a very good friend.

I profoundly appreciate and thankful to Prof. Damaschke and Dr Schaeper for guiding me through the course of my thesis work and for the valuable time spent for me whenever I needed.

I am very grateful to have the support and guidance of Dr Baumgarten and particularly like to thank for the time spent with me and for proofreading my work.

This journey would not be so pleasurable without the support and love of my parents, Ramesh Babu and Radha Devi and the encouragement from my sister Dr Shanthi Sudha. I conclude my thesis by acknowledging the support of the woman behind me, Dr Lavanya.

Manoj Raman Kondabathula

Rostock, 11.05.2018